
TRIGGERING DARK SHOWERS WITH CONDITIONAL DUAL AUTO-ENCODERS

Luca Anzalone^{1,3}, Simranjit Singh Chhibra^{1,2,5}, Benedikt Maier^{2,4}, Nadezda Chernyavskaya², Maurizio Pierini²

¹Department of Physics and Astronomy (DIFA), University of Bologna, Bologna, Italy

²European Organization for Nuclear Research (CERN), Geneva, Switzerland

³Istituto Nazionale di Fisica Nucleare (INFN), Sezione di Bologna, Italy

⁴Karlsruhe Institute of Technology (KIT), Karlsruhe, Germany

⁵Queen Mary University of London (QMUL), London, UK

ABSTRACT

Auto-encoders (AEs) have the potential to be effective and generic tools for new physics searches at colliders, requiring little to no model-dependent assumptions. New hypothetical physics signals can be considered anomalies that deviate from the well-known background processes generally expected to describe the whole dataset. We present a search formulated as an anomaly detection (AD) problem, using an AE to define a criterion to decide about the physics nature of an event. In this work, we perform an AD search for manifestations of a dark version of strong force using raw detector images, which are large and very sparse, without leveraging any physics-based pre-processing or assumption on the signals. We propose a dual-encoder design which can learn a compact latent space through conditioning. In the context of multiple AD metrics, we present a clear improvement over competitive baselines and prior approaches. It is the first time that an AE is shown to exhibit excellent discrimination against multiple dark shower models, illustrating the suitability of this method as a performant, model-independent algorithm to deploy, e.g., in the trigger stage of LHC experiments such as ATLAS and CMS.

1 Introduction

Data-driven, model-independent analyses are becoming a valid alternative to signal-dependent searches aimed at finding new physics Beyond the Standard Model (BSM). Since BSM physics is governed by a vast parameter space, the number of model-dependent analyses is substantial with conventional search techniques, as they typically target a specific signal scenario. These conventional searches can be either conducted *manually* or in a data-driven fashion. The *cut-based* approach involves physics experts inspecting the distributions of various physical variables to find discriminating characteristics¹. Once identified, the best threshold (in jargon called the *best cut*) is determined above which events are considered to be signal-like. This part of the analysis can be automatized by training a Machine Learning (ML) [1] or Deep Learning (DL) classifier [2, 3, 4] separating simulated background and signal events. Subsequently, a rigorous statistical test [5] is performed to determine the statistical significance of the classified signal: if the significance is above a certain value, the signal is said to exist; if too low, the signal can be confidently excluded to exist at all.

Both the cut- and supervised ML-based search strategies are *model-dependent*, i.e., they assume a particular scenario for new physics, thus being signal-specific. Moreover, the classifier inherently adapts its learned parameters to be sensitive to the specific features that describe the signal, therefore it does not necessarily generalize towards unknown signals. Moreover, a supervised approach requires accurate simulations of the signal and background and robustness against systematic uncertainties. Instead, we propose a *model-independent* search strategy powered by Auto-Encoders (AEs) [6, 7] and Anomaly Detection (AD) [8, 9, 10, 11, 12, 13, 14] that can help overcome such limitations by being more

¹The aim of a search is to discard as many *background* events as possible while preserving the most *signal*: the background represents what is already well known to exist, i.e., background from Standard Model processes or from instrumentation effects. The signal, which may or may not exist in Nature, is the object of the search. The scope of the analysis is to determine how plausible the existence of a specific signal is.

robust and able to adapt to the specific background(s), as well as generalizing multiple signals despite experiencing any training data for them.

In this article we focus on two important, challenging manifestations of Hidden Valley models [15], more specifically, of dark quantum chromodynamics, namely Semi-Visible Jets (SVJs) [16, 17, 18] and Soft Unclustered Energy Patterns (SUEPs) [19], introduced in the next section. We present a deep auto-encoder model that can detect both SUEP and SVJ signals in detector images constructed from trigger-level information, distinguishing them from SM multijet background, within the time budget of 100 ms available at the online selection step of the High Level Trigger (HLT) system [20]. The whole task is framed as a *normal-only anomaly detection* problem, in which the QCD background represents the *normal* class of data, whereas the two signals are treated as *anomalies*. Our contributions can be summarized as follows:

- We frame the new physics search problem as a normal-only anomaly detection task, making no assumptions on the nature of the signals, based on raw and mostly *sparse* detector images without the need for a problem-specific heavy pre-processing. The anomaly detection criterion is provided by an auto-encoder trained only on background data, comparing its performance on latent-based and reconstruction-based anomaly scores.
- We propose a novel architectural method for learning an *auxiliary latent space* that is compact enough to be visualized and also employed for anomaly detection. This is combined with (variational) auto-encoders, resulting in a *dual-encoder* design that makes use of *spatial conditioning*. We show the auxiliary latent space captures intrinsic information of the input images.
- We study how to best leverage the raw detector images of energy deposits, showing how we can “feature-engineer images” to enhance the discrimination performance of the AE, without the need for high-level features.

Our approach can potentially enable generic physics searches for unknown, new signals just from raw detector images of particle collisions. The only assumption we made is to have a dataset of only normal samples: instead, both weakly-supervised (e.g., [21]) and classification [2, 3] methods assume a partial or full knowledge of the signal(s), making the whole analysis far more complicated and signal-specific. Moreover, learning directly from detector images does not require any specific knowledge of the underlying physics objects and quantities (e.g. particles, jets), removing the need for search-specific data pre-processing, on which discrimination performance can be highly dependent [22]. By generalizing across multiple theorized manifestations of new physics, one therefore also achieves a simplification of the analysis setup. Moreover, the novel conditional dual-encoder architecture can learn a 2D auxiliary latent space that can be visualized and interpreted and directly used to construct anomaly scores. This new auto-encoder architecture allows for accurate latent-based AD that only requires forwarding the smaller encoder network (instead of the full model), rendering it more suitable for compression, acceleration, and deployment for trigger-level, or even real-time, applications with strict latency requirements.

1.1 New Physics Search Scenario

Hidden valley (HV) models [15] are a type of BSM physics describing the possible existence of a new sector of particles and forces with new gauge groups and a mediator to the Standard Model that can be produced at the Large Hadron Collider (LHC) [23]. HV models postulate a rich palette of particles in a hidden, dark sector, interacting via dark forces such as dark QCD. In some manifestations, these models generate a high-multiplicity final state after a dark showering and hadronization process similar to the SM QCD sector. Hidden valleys have been developed to address the origin of dark matter [24], whose signatures often feature non-isolated objects with high-multiplicity and/or soft final states, representing a challenging target for existing analyses at the LHC [25]. Dark matter provides one of the strongest motivations for physics beyond the Standard Model, and confirming its existence is one of the core missions of the LHC program.

HV can produce dark quarks in proton-proton collisions at the LHC, leading to a dark shower and the production of a large number of dark hadrons (ϕ_D), analogous to QCD jets [15, 19]. Depending on the details of the theory, the dark showers can follow large-angle emission and dark hadrons do not arrange in narrow QCD-like jets. The decay of dark hadrons results in dark photons (Z_D), which further decay to low-energy SM particles with transverse energy (E_T) of $\mathcal{O}(10^2)$ MeV, the final experimental signature being high-multiplicity spherically-symmetric soft unclustered energy patterns [19]. Through their decay to SM particles via some portal state, like a dark photon, these processes become visible and in principle detectable in 4π -detectors at the LHC such as ATLAS [26] and CMS [27]. We focus on a well-motivated scenario where SUEP is produced in exotic Higgs (H) boson decays via gluon-gluon fusion and all dark hadrons decay promptly and exclusively to pions and leptons, an experimental nightmare scenario because of an overwhelming multi-jet QCD background.

Another manifestation of hidden valleys can be semi-visible jets [18, 16], a phenomenon in which energetic particles are emitted in a spray of stable invisible dark matter along with unstable states that decay back to SM. These showers

are partially detectable, with the visible components looking like QCD showers [16]. This partial visibility makes it challenging to identify and study these particles thoroughly, having a low acceptance with current methods.

Searches for SVJ or SUEP signatures can potentially shed new light on the existence of dark matter and novel hidden sectors as well, which are currently uncovered and undercover at the LHC. Moreover, the richness in model parameters in dark QCD scenarios and the changes in kinematic properties due to parameter variations make an efficient, model-independent identification of dark QCD signatures the ultimate goal of such analyses.

1.2 The CMS Detector and simulated samples

The CMS experiment [27] is designed to explore the physics of proton-proton collisions through a system of different sub-detectors, each designed to measure different aspects of the particles produced in a collision. Given its *cylindrical* design, it is often convenient to adopt a polar coordinate system (θ, ϕ) where: $0 \leq \theta \leq \pi$ is the polar angle, and $0 \leq \phi \leq 2\pi$ is the azimuthal angle. From these coordinates is possible to explain the particle’s kinematic as (p_T, y, ϕ, m) : where m is the invariant mass, p_T the transverse momentum, and y the rapidity. A quantity related to the rapidity is the *pseudorapidity* η , which is a measure of the angle of the particle’s motion relative to the beam line. The images employed in our study are represented in the η - ϕ plane.

The CMS detector consists of several layers that are used to measure various properties of particles produced in high-energy collisions. The ones relevant to our work are the:

- **Inner tracking system** [28]: measures the momentum of particles by their curvature radius through the magnetic field. The tracker can monitor the paths of charged particles. This sub-detector covers a pseudorapidity region of up to $|\eta| < 2.5$, being made of 66M silicon pixel detectors ($100 \times 150 \mu m^2$ in size) for accurate measurement of the particle’s trajectory.
- **Calorimeters**: consisting of an Electromagnetic calorimeter (ECAL) [29], and a Hadron calorimeter (HCAL) [30]. The calorimeters can measure the direction and energy of both charged and neutral particles. The two sub-detectors have different granularity: for the ECAL, the granularity of $0.0174 \times 0.0174 \text{ rad}^2$ results in $286\eta \times 360\phi$ bins for the size of the images, whereas the HCAL is 25 times less granular, i.e., $0.087 \times 0.087 \text{ rad}^2$. Therefore, each HCAL image is upsampled by a factor of 25 in the preprocessing step, giving 1/25th of the energy to each pixel.

We employ the Delphes v.3.4.3pre1 fast detector simulation [31] with the CMS Run-2 detector model to obtain the tracker, ECAL, and HCAL images. Samples of SM multijet events as well as for SVJ and SUEP signal processes have been generated with the Pythia v8.244 event generator [32, 33].

2 Related Work

In this section, we introduce the class of neural network models that we employ and provide an overview of the works relevant to our study.

2.1 Auto-Encoders and Variations

Auto-encoders (AEs) [34, 7] are self-supervised models made of three components: the *encoder* network $f_\phi(x)$, the *bottleneck* (or latent space) z , and the *decoder* network $p_\theta(z)$. The encoder compresses the input x to a latent representation $z = f_\phi(x)$ from which the decoder tries to reconstruct the input $\hat{x} = p_\theta(z)$ such that $\hat{x} \approx x$. Notably, auto-encoders have been applied to dimensionality reduction [34], denoising [35], classification, clustering, recommendation systems, and anomaly detection [36] tasks as well.

Variational AE. A variational auto-encoder (VAE) [6] is a deep generative model in which both encoder $q_\phi(z | x)$ and decoder $p_\theta(x | z)$ networks are now probabilistic models learned by amortized variational inference. The VAE commonly assumes the latent space to be governed by a multivariate Gaussian distribution $z \sim \mathcal{N}(\mu_\phi, \sigma_\phi^2 I)$ that is parameterized by the encoder: $\mu_\phi, \sigma_\phi^2 = q_\phi(x)$, where I is the identity matrix. To learn the model parameters (ϕ, θ) the VAE is trained to minimize the *evidence lower-bound* (ELBO):

$$\mathcal{L}_{\phi, \theta}(x) = \mathbb{E}_{z \sim q_\phi(x)} [\log p_\theta(x | z)] + \beta D_{KL}(q_\phi(z | x) \| p(z)). \quad (1)$$

The first term maximizes the likelihood of the reconstructed samples from the decoding distribution, while the Kullback-Leibler divergence (D_{KL}) penalizes the encoding distribution for being far from the prior distribution, usually an isotropic Gaussian $p(z) = \mathcal{N}(0, I)$. Moreover, the hyperparameter β can be adjusted to introduce a constraint on

the capacity of the latent space, encouraging q_ϕ to match the prior $p(z)$ more closely: high values of β can lead to a trade-off between the reconstruction quality and disentangled latent codes, which can better explain the underlying factors of variations that govern the true data distribution [37].

Categorical VAEs. The regular VAE can capture only continuous features in its latent bottleneck, the Categorical VAE, instead, is capable of learning *discrete* latent variables by letting the encoder parameterize a relaxation of the Categorical² distribution called the *Gumbel-Softmax* [38] or the *Concrete* [39] distribution: denoting such distribution $Cat(\alpha, \tau)$, the degree of relaxation is controlled by the temperature parameter $\tau \in (0, \infty)$ that allows interpolating, in the limit, between a Uniform ($\tau \rightarrow \infty$) and a true Categorical ($\tau \rightarrow 0$), where the *logits* α specify the unnormalized log-probabilities over C discrete categories. The hyperparameter τ can be difficult to set properly, for such reason common approaches are either to: fix the value between 0.1 and 1 [40], anneal it from high to a low target value [41], or even learn it with a shallow neural network [42, 43]. We opt for the learnable option since it provides more flexibility for the whole model, as the temperature can freely adapt during training. A Categorical VAE is trained to minimize the ELBO as in Eq. 1, in which the prior is now uniformly distributed over the categories: $p(z) = Cat(\log 1/C)$; the reparameterization of the latents happen by means of the *Gumbel-Max trick* [38, 39]:

$$z = \text{softmax} \left(\frac{\alpha_\phi + g}{\tau} \right), \quad (2)$$

where $\alpha_\phi = q_\phi(x)$, and the Gumbel noise g is obtained by inverse sampling from a Uniform distribution: $g = -\log(-\log u)$, where $u \sim U(0, 1)$. The trick makes use of a `softmax` approximation of the `max` in order to be fully differentiable. Like the VAE, both classes of models can *generate* new samples \tilde{x} that are expected to follow the training data distribution by decoding from latent vectors sampled from the prior: $\tilde{x} = p_\theta(\tilde{z})$, where $\tilde{z} \sim p(z)$.

Variations. Further modifications of the regular VAE can employ: a conditional prior $p(z | c)$ on representations c to enable structured generation [44], a Gaussian-mixture prior to allow handling more complex data [45], and even a combination of both continuous and discrete latent spaces [46] to capture both kinds of features.

2.2 Anomaly Detection

Anomaly detection (AD) [47] is the task of determining which samples violate some notion of normal behavior: once identified, such samples will be referred to as *outliers* or *anomalies*. AD can be performed in different settings, but we assume a normal-only set of samples: *being a good approximation to what occurs in practice, i.e. having the background contaminated with a little fraction of unknown signals*. Auto-encoders are a popular mean to perform anomaly detection: the AE is usually trained to maximize the reconstruction quality of the normal samples, by minimizing a mean squared objective. Then, the trained AE is evaluated on all samples, hoping the outliers are poorly reconstructed. For these samples, the reconstruction error should be higher than a threshold (determined on a validation set), signaling the abnormality of such data. A general challenge is about how to determine or devise anomaly scores or metrics that best separate the normal data from the anomalies [48]; AEs allow conceiving two classes of anomaly scores, according to whether they are based on the learned latent space or defined from the reconstructed samples. Other notable approaches to perform anomaly detection are one-class methods [49], Isolation Forests [50], and the ones based on generative adversarial networks [51].

Reconstruction-based. Heimel et al. [8] introduce the benchmark dataset of QCD vs top jets, in which they studied the problem from a particle-based point of view, training auto-encoders to reconstruct either jet images or constituents 4-momenta vectors. Their approach heavily relies on specific processing that transforms raw collisions into particles (high-level physics objects), greatly simplifying the problem. Before training their models, the authors employ a powerful pre-processing step in which the jets are first centered, rotated, and mirrored before yielding 40×40 cropped images which are further normalized to sum to one. They demonstrate that their LoLa auto-encoder based on 51 extended 4-vectors, that introduce knowledge about jet-level kinematics, is able to beat the image-based AE by a large margin even with a smaller latent space, although at the cost of introducing an even larger dependency on the jet mass. Finke et al. [11], instead, discuss the limitations of using AE on the same kind of data. The authors claim that "due to the sparsity and the specific structure of the jet images, the auto-encoder fails to tag QCD jets if it is trained on top jets". This problem is known as *complexity bias* and is partially explained by a correlation between the reconstruction loss and the number of non-zero pixels in the images, as the loss tends to increase when the number of non-zero pixels is higher. For this reason, they introduce the kernel-MSE as a loss function, that is less sensitive than MSE while encouraging the network to learn the structure of the inputs. The authors also compare the performance of their AEs against various intensity remapping functions, used to alter the pixel values of the input images. Both

²The Categorical distribution generalizes the Bernoulli over C categories, with $C > 2$.

improvements enabled the authors’ AE to learn even dim pixels. Recently, Dillon et al. [12] propose to use a normalized auto-encoder (NAE) [52] to overcome the complexity bias, thus identifying anomalous jets symmetrically. The NAE is trained to maximize the likelihood of the data, through the minimization of an energy function (corresponding to the reconstruction error) used to define a Gibbs distribution, representing its probability density. Under this probabilistic formulation, the NAE is forced to inhibit the reconstruction of an outlier, since it has to maximize the likelihood of the training data, guaranteeing low reconstruction error only for such data. Although, NAEs are well-suited for anomaly detection, avoiding their training instabilities is still a practical challenge.

Latent space-based. Dillon et al. [21] propose to use a Dirichlet VAE [53] to learn a bi-modal, 1d latent space that naturally encodes the two classes. The authors show that the Dirichlet prior on the latent space naturally leads to mode separation, something that was not observed for both the regular VAE [6] and the Gaussian-mixture VAE [45], without enforcing any additional loss term. The proposed Dirichlet VAE reaches high class separation performance although weak-supervision is still assumed, and its decoder’s weights also show some degree of interpretability. Bortolato et al. [13], instead, propose to use the Kullback-Leibler divergence (KLD) between the learned and prior Gaussian distributions as an anomaly metric to detect anomalous jets. Dillon et al. [54] compared the effectiveness of using low-dimensional latent space representations instead of the event space features to perform model-agnostic anomaly detection. They trained a transformer encoder [55] to optimize the JetCLR’s contrastive objective [56]. *Symmetry augmentations* were employed to define positive and negative pairs for the contrastive learning, such as rotation, distortion, and collinear split for jets, whereas randomly shifting in either η or ϕ directions for dijet events. Through a binary classification test, the authors found out that a sufficiently large latent space (e.g. of size 512) is required to encode the physical symmetries of jets. Finally, the CWoLa [57] method was used to perform model-agnostic anomaly detection, showing that still a significant fraction of signal events is required to achieve meaningful class separation. Govorkova et al. [58] demonstrate a real-world deployment of a VAE on FPGA hardware for real-time AD at the LHC [23]. The authors compared the performance of both reconstruction- and KL-based anomaly scores, for both AE and VAE models. They concluded that with a minor loss in performance, the scores based on the KL divergence allowed them to only deploy the VAE’s encoder on the FPGA, thus saving both hardware resources and latency costs. Our approach has a similar benefit: the computational cost can be reduced by more than half by deploying only the smaller, auxiliary encoder network. Recently, Cheng et al. [9] enhanced a VAE with a technique known as Outlier Exposure (OE) [59] that makes use of an auxiliary set of out-of-distribution (OOD) data to improve the sensitivity to anomalies. In particular, an auxiliary loss term is computed from OOD predictions, that is either defined as a classification loss in terms of MSE or a margin loss of the KL divergence between latent representations, which has ensured a good compromise between high separation of anomalies and jet mass decorrelation, conversely to distance correlation (DisCo) regularization [60, 61] that when applied to VAEs has a severe impact on discrimination performance. Although the promising results, it is not clear if data from the same physics domain is enough to be considered as OOD.

The analyses conducted in [14] and [10] are related to ours, because it is assumed a similar signal setting. In particular, Barron et al. [14] target the same SUEPs scenario in which the signal decays to exotic Higgs, and all the dark hadrons to SM hadrons. The authors identify three observables: charged particle multiplicity, event isotropy, and interparticle distance. These are used to build the input features for their unsupervised fully-connected auto-encoder. Canelli et al. [10], instead, study the SVJs signature by training a fully-connected auto-encoder on jet-level and jet substructure variables, minimizing the mean absolute error. Compared to these two studies, we neither rely on high-level nor engineered features but, instead, learn from detector images. Moreover, our models are evaluated against both signals, demonstrating anomaly scores that can identify both.

3 Dataset

The dataset contains $360 \times 286 \times 3$ images, for a total of about 615k samples, divided in: 442k QCD, 67k SUEPs, and 106k SVJs. The image channels represent two-dimensional E_T deposits in the η - ϕ plane, respectively, in the inner tracker (Trk), ECAL, and HCAL sub-detectors of CMS. Moreover, each image is annotated with a:

- **Class label.** There are three of them in total: the label 0 indicates the QCD background, the label 1 is associated to SUEP signal samples, and the label 2 refers to the second SVJ signal.
- **Mass label.** Signal samples only are identified by the mediator masses m_H [19] and $m_{Z'}$ [10] at which these were generated. In particular, SUEPs were generated at $m_H = \{125, 200, 300, 400, 700, 1000\}$ GeV and SVJs at $m_{Z'} = \{2.1, 3.1, 4.1\}$ TeV. For the rest of the paper, we refer to a particular signal sample by its mediator mass, such as SUEP(m_H GeV) and SVJ($m_{Z'}$ TeV).
- **Number of tracks variable.** This is a model-independent quantity that best approximates the number of decay products. We refer to this variable as nTracks. It should be noticed that this variable is obtained by track reconstruction, which is expensive, being not feasible for real-time inference at the HLT.

The split for QCD is 60% (training, 25% of them for validation) and 40% (test), whereas all the SUEP and SVJ events are used for testing: for the signals, an independent validation set was used for prior experimentation. More details about how events are generated and preselected are available in the appendices A.1 and A.2.

3.1 Data Pre-processing

Since the images are very sparse (around 99.4%) and also moderately large, we employ a simple pre-processing that down-scales the images, thus reducing sparsity while also preserving their total energy. As shown in algorithm 1 the down-scaling is performed by convolving a 5×5 kernel with all ones on the input images, in a non-overlapping manner with a stride equal to the kernel size, yielding a $25 \times$ reduction in spatial resolution while preserving the sum of the energy deposits: a kernel with all ones just sums E_T deposits depicted by each pixel; the resulting image resolution is now $72 \times 58 \times 3$, instead of $360 \times 286 \times 3$ (about 0.3Mpix). The reduction in resolution has many benefits: 1) the dataset is more manageable, since smaller, 2) the models will require less memory, parameters, and training time since they will be smaller and each convolutional layer will require less time to scan the down-sampled images, and 3) the sparsity is partially reduced (about 96%) because each new pixel value is now given by the sum of a 5×5 image patch.

Algorithm 1: Image Pre-processing

Input: a batch of images $I \in \mathbb{R}^{B \times H \times W \times C}$, kernel size K
Output: pre-processed images $I_M^{trk} \in \mathbb{R}^{B \times \lfloor H/K \rfloor \times \lfloor W/K \rfloor \times 1}$

```

/* Depthwise convolution to down-sample each channel by a factor of K */
1 kernel = tf.ones((K, K, C, 1))
2 I' = tf.nn.depthwise_conv2d(I, filter = kernel, strides = (1, K, K, 1), padding = "SAME")
/* Compute the mask image */
3 I_M = tf.cast(I' > 0, dtype = float)
/* Consider only the tracker channel, discarding the other two */
4 I_M^{trk} = I_M[... , 0, tf.newaxis]
5 return I_M^{trk}

```

In our prior experiments (discussed in section 5.5) we used to sum and normalize the E_T deposits over the tracker, ECAL, and HCAL channels, yielding one-channel images. We later discovered that the information that can be learned from energy deposits is not much discriminative for anomaly detection. Instead, as depicted by the last two steps in the pre-processing function 1, we devised a novel kind of image, that we call the *mask image* (described in section 4.1), using only the tracker channel that resulted in a way better discrimination performance in our search scenario.

3.2 Image Augmentations

Since our data have physical properties like total energy and the E_T deposits are arranged according to the design of the detector (other than being the result of a physics phenomenon), we cannot simply apply the usual off-the-shelf image augmentations like random crop, cutout, rotation, and jittering that would reorganize the image's pixels without following the underlying physics and also without preserving both the individual and overall value of E_T deposits. Instead, we design some novel data augmentations (as summarized in figure 1) that preserve the physical meaning of the images, working on the η - ϕ plane thus also respecting the detector's coordinates. In particular, one kind of image augmentation involves a flipping in η , while the other is a rotation in ϕ . The η -flip augmentation can be simply implemented by mirroring the x -axis from left to right, where the ϕ -rotation is a little more complex. Rotation in ϕ (i.e. along the y -axis³) can occur both upward and downward, in which a portion of the image moves up (or down) and the part in excess (the one that would fall off vertically from the image boundaries) is then attached to the bottom (or top). From a practical perspective, the ϕ -rotation is done in chunks of Δ rows, where the chunk size $\Delta = 8, 16, \dots, 56$ are only multiples of eight: a hyperparameter value found to work well experimentally.

By combining these two kinds of image augmentations, flipping and rotation, it is possible to yield a total of five combinations of augmentations: 1) upward rotation, 2) downward rotation, 3) flipping, 4) flipping and upward rotation, and lastly 5) flipping with downward rotation. These augmentations can be generally applied to any model (e.g. classifiers, regressors, etc) that learns from images, being not anomaly detection specific, encouraging them to both generalize and learn properties about the detector coordinate space.

³We refer to Cartesian x and y axes in the context of images, rather than x and y as detector coordinates.

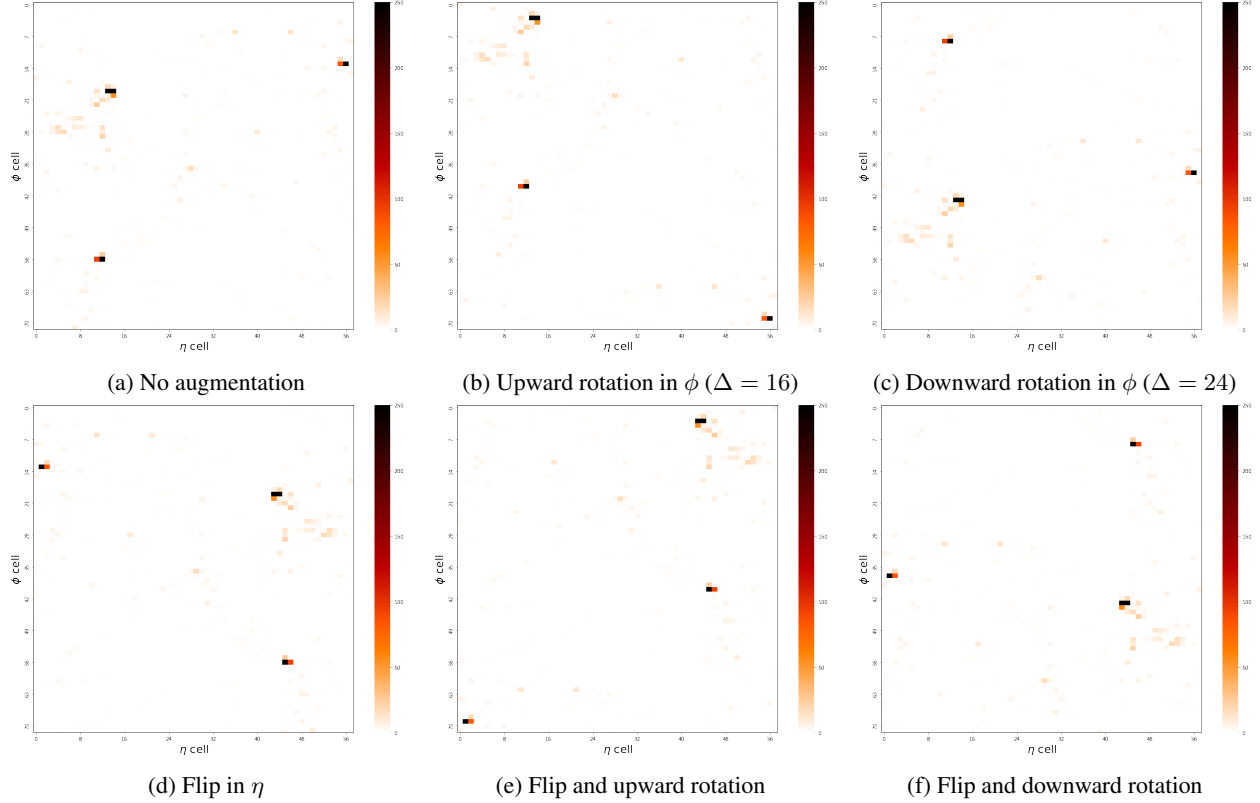


Figure 1: Example of five kinds of data augmentations, demonstrated on a random QCD sample.

4 Method

We propose a *conditional dual auto-encoder* model architecture to perform a normal-only anomaly detection from raw detector images depicting energy deposits of particle collisions. As the name suggests, our model comprises *two* encoders: a high-capacity one responsible for capturing pixel-level details in a large convolutional bottleneck, and a second *auxiliary* encoder whose task is to compress its input image to a small but discriminative latent space. We denote the large latent space by Z and the smaller one with Z_m . Then, the decoder network has to reconstruct the input image from Z while being *spatially conditioned* on Z_m . Conditioning occurs at different levels of the network hierarchy, starting from Z and then influencing the hidden features at each up-sampling stage. Moreover, thanks to the large latent space our model is able to pixel-accurate image reconstructions, and plausible generations for the variational variant. Moreover, each component of the auxiliary Z_m serves as a latent-based anomaly score, in addition to the reconstruction-based ones.

4.1 The Dual Encoders

As we want to capture both the detail and discriminative features, we define two encoders: one is residual (f_R), and the other is convolutional (f_m). Each encoder has a different architecture, to introduce a prior when learning the features encoded in the bottleneck, yielding two separate latent spaces: respectively, Z with high capacity and Z_m with typically two components. Both networks receive as input the mask image of the tracker channel, instead of energy deposits.

Mask image. The mask image (I_m) in figure 2 has Boolean values obtained from the original image (I) of E_T deposits, just by determining whether or not a pixel depicts a non-zero energy value⁴: $I_m = \mathbf{1}[I > 0]$, where $\mathbf{1}[\cdot]$ is an indicator function applied to each pixel of I ; this can be seen as a sort of *image feature engineering*. Each mask image, if summed, denotes the number of non-zero deposits associated with sensors in the detector, that measured some energy. Such quantity is related to the nTracks variable, but not equivalent since, depending on the granularity used to yield the images, two or more tracks can fall in the same bin (pixel) thus being not distinguished when counting non-zero pixels.

⁴Even without the pre-processing step, all the energy values are always non-negative.

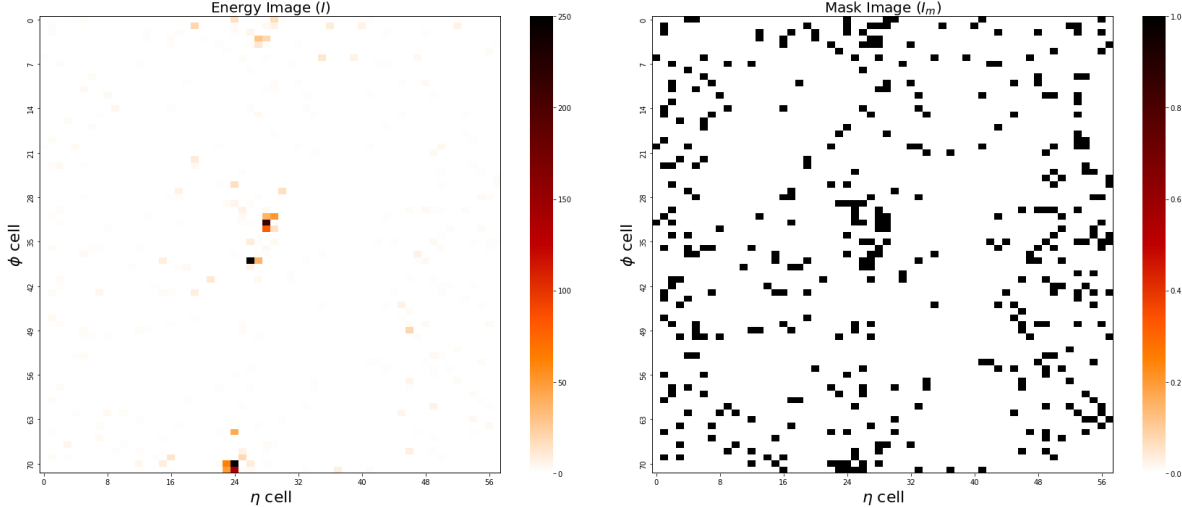


Figure 2: Energy (left) and mask (right) images of a single sample.

Input	Operator	Filters	Strides	Groups	# Conv
$72 \times 58 \times 1$	conv_blk	64	2	1	1
$36 \times 29 \times 64$	residual	64	1	4	2
$36 \times 29 \times 64$	conv_blk	128	2	4	1
$18 \times 15 \times 128$	residual	128	1	4	2
$18 \times 15 \times 128$	conv_blk	128	2	4	1
$9 \times 8 \times 128$	residual	128	1	4	2
$9 \times 8 \times 128$	conv_blk	256	2	4	1
$5 \times 4 \times 256$	residual	256	1	4	2
$5 \times 4 \times 64$	conv1x1	64	1	1	1

Table 1: Architecture of the residual encoder, f_R . The operator conv_blk denotes a convolutional block made of a 2d convolution followed by instance normalization [64], with the Leaky-ReLU [68] activation ($\alpha = 0.2$) at the end. Instead, the residual operator comprises two conv_blk blocks, plus a skip connection. All the convolutions have a 3×3 kernel size. Down-sampling is performed by strided convolutions, instead of pooling. The last point-wise convolution [69] (conv1x1) linearly combines the feature maps to yield the $5 \times 4 \times 64$ latent space.

In particular, for training our models, we consider the mask image computed from the energy deposits of the tracker channel only. These kinds of images proved to be more discriminative than the energy ones for the two signals object of this search. Moreover, pixels in I_m are naturally normalized being either zero or one, avoiding the need of normalizing E_T deposits which are large in range and skewed towards small values.

Architectures. The network f_R is residual-like [62], following some of the practices suggested in [63]: as applying instance normalization [64] after each convolution, which resulted in higher image quality compared to batch normalization [65]. Differently from [63], we use grouped convolutions [66, 67] to reduce the number of learnable parameters. The network architecture is detailed in table 1, resulting in about 612k parameters. The residual encoder transforms the tracker mask images I_m to a large convolutional bottleneck, i.e. $Z = f_R(I_m)$ where $|Z| = 5 \times 4 \times 64$, to provide enough details for pixel-accurate reconstructions.

The convolutional encoder, f_m , has a different architecture than f_R being smaller and lacking residual connections, as detailed in table 2. The network f_m has about 270k parameters, encoding the mask images I_m within the discriminative 2d latent space, i.e. $Z_m = f_m(I_m)$ where $|Z_m| = 2$. We will call f_m the *mask encoder*.

4.2 The Conditional Decoder

The conditional decoder D is a residual-like [62] network whose main input is the convolutional bottleneck, Z (i.e. the output of the residual encoder, f_R), from which it tries to reconstruct the input mask images, I_m . The large Z provides

Input	Operator	Filters	Strides	Groups
$72 \times 58 \times 1$	conv_blk	64	1	1
$72 \times 58 \times 64$	max_pool	-	2	-
$36 \times 29 \times 64$	conv_blk	128	1	2
$36 \times 29 \times 128$	max_pool	-	2	-
$18 \times 15 \times 128$	conv_blk	128	1	2
$18 \times 15 \times 128$	max_pool	-	2	-
$9 \times 8 \times 128$	conv_blk	256	1	2
$9 \times 8 \times 256$	max_pool	-	2	-
$5 \times 4 \times 256$	flatten	-	-	-
5120	dense	2	-	-

Table 2: Architecture of the convolutional encoder, f_m . Overlapping Max-Pooling (max_pool) is employed to reduce the spatial dimensions by a factor of two, having a 3×3 kernel. When the features maps are small enough, a flatten operation reshapes them to a rank-1 tensor, and a final fully-connected (dense) layer yields the latent space of size two.

Input	Operator	Filters	Strides	Groups	# Conv
$5 \times 4 \times 64$	conditioning	-	-	-	-
$5 \times 4 \times 256$	up-conv_blk	256	1	4	1
$10 \times 8 \times 256$	residual	256	1	4	2
$10 \times 8 \times 256$	conditioning	-	-	-	-
$10 \times 8 \times 256$	up-conv_blk	128	1	4	1
$20 \times 16 \times 128$	residual	128	1	4	2
$20 \times 16 \times 128$	conditioning	-	-	-	-
$20 \times 16 \times 128$	up-conv_blk	128	1	4	1
$40 \times 32 \times 128$	residual	128	1	4	2
$40 \times 32 \times 128$	conditioning	-	-	-	-
$40 \times 32 \times 128$	up-conv_blk	64	1	4	1
$80 \times 64 \times 64$	residual	64	1	4	2
$80 \times 64 \times 64$	crop	-	-	-	-
$72 \times 58 \times 64$	conv1x1	1	1	1	1

Table 3: Architecture of the conditional decoder D . Conditioning occurs at the input level as well as at multiple spatial resolutions. The up-conv_blk denotes a block that comprises a 2×2 bilinear up-sampling operation, followed by a 2d grouped convolution and instance normalization, similarly to conv_blk. Since the up-sampled feature maps get larger than the input images, we employ a center crop operation (crop) to obtain matching sizes. The final conv1x1 outputs $72 \times 58 \times 1$ images by a sigmoid activation.

alone enough information for D to enable high-quality reconstructions, but the question is about how to enable the mask encoder f_m to learn a compact latent space, Z_m . The answer is provided by *conditioning* [70], which establishes a dependency between the decoder D and the auxiliary latent space, Z_m , that allows the gradients of the loss to flow through f_m without any direct supervision. The decoder architecture is summarized in table 3, which results in about 760k trainable parameters; we call the whole auto-encoder architecture a *Conditional Dual Auto-Encoder* (CoDAE).

During training, the conditioning mechanism propagates the reconstruction error also to the mask encoder, providing feedback to learn Z_m such as to maximize the reconstruction quality. Turns out that Z_m alone is not enough for pixel-accurate reconstructions⁵, and so we also need to learn the high-capacity latent space Z . Intuitively, we write $\hat{I}_m = D(Z | Z_m)$ to highlight that the compact bottleneck Z_m must influence the reconstructions \hat{I}_m , in order to represent meaningful and not just random encoded features. For such reason, the conditioning should be strong enough to prevent D from completely relying only on the large Z , and so we apply it in terms of multiplicative interactions [70] that occur at multiple levels of the decoder hierarchy.

⁵Even with a high-capacity residual encoder, reconstructing from only the two components of Z_m results in reconstructions that look like just *average images*, instead, thus without pixel-level details.

Our form of conditioning combines spatial broadcast [71] with a feature-wise transformation [70]: element-wise multiplication. We will refer to such operation as *spatial conditioning* (algorithm 2): the spatial broadcast provides a bias to the convolutional encoder (f_m) for learning disentangled latent factors in Z_m , while, at the same time, modulating Z and the subsequent hidden feature maps. Algorithm 2 is called multiple times, as we condition at multiple spatial scales of the decoder’s hierarchy of layers. Initially, at stage $i = 0$, the conditioning is performed on Z itself (i.e. $h_0 = Z$) which is then fed to the first layers of the decoder. Subsequently ($i > 0$), but right before each `up-conv_blk`, also the hidden feature maps (output of the previous `residual` block in stage $i - 1$), h_i , are conditioned on the same Z_m . In this way, the mask latent space Z_m effectively modulate the decoder at different spatial resolutions. In general, our spatial conditioning algorithm is not limited to only multiplicative interactions. Other simple conditioning mechanisms applied on feature maps are possible, like addition (or biasing), concatenation, or even an affine-like operation that combines both multiplication (also known as scaling) and biasing.

Algorithm 2: Spatial Multiplicative Conditioning

Input: latents $Z_m \in \mathbb{R}^2$, tensor $h_i \in \mathbb{R}^{H \times W \times C}$, kernel size K
Output: spatially conditioned representation $r \in \mathbb{R}^{H \times W \times C}$

```

/* See algorithm 1 in [71] */
1  $z = \text{SpatialBroadcast}(Z_m, W, H)$  */
/* Expand channels of  $z$  to match  $h_i$ , through a linear convolution */
2  $z = \text{Conv2D}(\text{filters} = C, \text{kernel\_size} = K, \text{padding} = \text{'same'})(z)$  */
/* Multiplicative conditioning: Hadamard product  $z \odot h_i$  */
3  $r = \text{tf.multiply}(z, h_i)$ 
4 return  $r$ 

```

Training. During training, we make use of the set of augmentation functions \mathcal{T} defined in section 3.2. At each mini-batch of mask images I_m a random augmentation is sampled $t \sim \mathcal{T}$ and applied to it, the augmented images $\tilde{I} = t(I_m)$ are then fed to both residual and mask encoders; the decoder is then trained to reconstruct \tilde{I} . Data augmentations enable the CoDAE models to learn invariances related to the coordinates η and ϕ of the detector. In addition, we perform model selection according to the value of the *structural similarity* [72] metric between the true and reconstructed images, computed on a validation set.

The whole AE model is learned end-to-end using the AdamW optimizer [73], whose learning rule decouples the weight decay regularization term from the main objective [74] making it easier to tune, minimizing the binary cross-entropy loss⁶. The optimizer is left with default parameters and learning rate, except for the weight decay coefficient set to 10^{-4} . Furthermore, to improve training stability, we limit the l_2 -norm of each gradient to be at most one. Lastly, all the weights are initialized by following the `he_uniform` [75] scheme with zeros biases except for the decoder, whose biases are initialized to -1 to provide a better starting point for the initial reconstructions.

4.3 Categorical CoDVAE

The described CoDAE architecture can be extended to variational auto-encoders [6]. In particular, we explored the Categorical VAE [39, 38] in which the large latents are now sampled from a Gumbel-Softmax distribution, $Z \sim \text{Cat}(\alpha_R, \tau_R)$, where $\alpha_R, \tau_R = f_R(I_m)$ are the learned logits and temperature; we call this model the *Categorical Conditional Dual Variational Auto-Encoder*, or CoDVAE in short. Likewise, in previous approaches [42, 43], we let the residual encoder also output a temperature τ_R that defines the degree of relaxations of the Categorical distribution parameterized by α_R . Basically, we add a second point-wise convolution (`conv1x1`), with a softplus activation⁷ to ensure positive values, on the latest `residual` block of table 1, plus a base temperature τ_0 which is a hyperparameter set to 1. Since we learn the temperature, we define a more complex prior $p(Z)$ as a uniform mixture of N Gumbel-Softmax with different temperatures sampled uniformly in $[0.1, 1]$, to provide more flexibility to the latent space:

$$p(Z) = \frac{1}{N} \sum_i^N \text{Cat}(\log 1/C, \tau_i), \quad \tau_i \sim U(0.1, 1) \quad (3)$$

⁶The loss is summed over spatial dimensions (height, width, and channels), and averaged over the batch size.

⁷The softplus is defined as $f(x) = \log(1 + \exp(x))$.

We then approximate the KL divergence (D_{KL}) between the prior and the learned distribution, $q = \text{Cat}(\alpha_R, \tau_R)$, with a Monte-Carlo estimate ($M = 10$), as follows:

$$D_{KL}(q \parallel p) \approx \frac{1}{M} \sum_{z \sim q(x)}^M \log q(z \mid x) - \log p(z). \quad (4)$$

To enable sharp reconstructions of mask images, we opt for learning a probabilistic decoder in which each output pixel is independently governed by a Bernoulli distribution: able to represent pixel values that are either zero or one, as in I_m . A single Bernoulli distribution can be denoted as $\text{Bern}(p_\theta)$ where p_θ is learned, and specific for a single pixel. For sharp predictions we take the *mode* of such distribution since it is 1 if $p_\theta > \frac{1}{2}$ and 0 otherwise: its mean, instead, is suitable to represent smooth values in $[0, 1]$ like a normalized energy deposit.

4.4 Anomaly Scores

Auto-encoders provide the opportunity to define a variety of scores to perform anomaly detection. We can classify them into two main categories: latent- and reconstruction-based.

Latent-based. Anomaly scores are defined from the latent space captured by the encoder network. In the case of AEs, directly using the learned bottleneck can be difficult since it is usually high-dimensional, and so combining the information carried by each latent component into a single score can be challenging without using explicit supervision (e.g. training a latent classifier.) Instead, in our CoDAE architecture we avoid this issue by training a second auxiliary latent space, $Z_m = f_m(x)$, that is low-dimensional, allowing each component to be an anomaly score: in our case $|Z_m| = 2$, so we obtain two AD scores. In addition to this, VAEs provide a natural way to discriminate on the latent space through the KL divergence between the learned posterior and the prior distribution, i.e. $D_{KL}(q(z \mid x) \parallel p(z))$. Yet another option is provided by the fact that the KL-divergence is not *symmetrical*: $D_{KL}(q \parallel p)$ and $D_{KL}(p \parallel q)$ have two different meaning, the former promotes mode-seeking behavior (called the *reverse* KL) and the latter encourages coverage of probability mass (known as *forward* KL). We exploit these two additional scores (denoted as KL-R and KL-F) with our Categorical CoDVAE model.

Reconstruction-based. Anomaly scores are obtained by comparing the reconstructions \hat{x} with the inputs x of the AE. Different scores can be determined according to the distance or similarity function used to compare images: for ease of notation, we denote the set of pixels $P \in \mathbb{R}^{H \times W \times C}$ of an image and define our scores on that. In particular, we evaluate the following reconstruction-based scores:

- $\text{BCE}(x, \hat{x}) = -\sum_{p \in P} x_p \log \hat{x}_p + (1 - x_p) \log 1 - \hat{x}_p$. Denotes the sum of the *binary-cross entropy* between the true and predicted pixels, which we also use as a loss function for training our models. Since the pixel values in each mask image are either zero or one, this measure is well-defined, without any normalization.
- $\text{SSE}(x, \hat{x}) = \sum_{p \in P} (x_p - \hat{x}_p)^2$. Represents the *sum of squared errors* between the true and reconstructed pixels. This quantity is similar to the MSE, except that it is computed per sample thus without averaging over the batch size.
- $\text{SAE}(x, \hat{x}) = \sum_{p \in P} |x_p - \hat{x}_p|$. Depicts the *sum of absolute errors*, which is the absolute difference between true and predicted pixels. It is worth noticing that if the Categorical CoDVAE model is evaluated on mask images, this metric is equal to the SSE since both squared and absolute differences can be either zero or one (according to whether the pixel is correctly predicted or not): this is a direct consequence of taking the mode of the learned Bernoulli decoder, whose output' pixels are exactly zero or one. Thus, in such cases, we omit the results of the SAE scores. Moreover, we can define SAE on mask images too: $\text{SAE-mask}(x, \hat{x}) = \sum_p |1[x_p > 0] - 1[\hat{x}_p > 0]|$.
- $\text{Dice}(x, \hat{x}) = \frac{\sum_{p \in P} x_p^2 + \sum_{p \in P} \hat{x}_p^2}{2 \sum_{p \in P} x_p \cdot \hat{x}_p}$. This score is defined as the inverse of the Dice coefficient [76], to provide a measure of dissimilarity between two sets of pixels: x and \hat{x} .
- $\text{PixelSum}(x, \hat{x}) = \sum_{p \in P} \hat{x}_p$. Defined as just the sum of each predicted pixel value. This score can be interpreted as *predicted total energy* if the AE is trained to reconstruct I (energy image), or as an approximation of the nTracks if reconstructing I_m (mask image), instead. We also investigated the total number of predicted non-zero pixels, i.e. $\sum_p 1[x_p > 0]$, but we did not report results about it because its discriminatory capability is relatively weak.

Both categories of anomaly scores have their pros and cons. Reconstruction scores are in general easier to define, for example from either common loss functions or metrics, but to compute them it is required to forward the full model

(encoder and decoder) since we need to reconstruct the samples. Instead, latent-based scores involve only the encoder predictions being more suited for inference, although possibly more difficult to define (e.g. analytical or empirical KL) and visualize (e.g. dimensionality reduction on high-dimensional latent space.)

5 Results

In this section we first describe the evaluation metrics and baseline methods used to compare our approach against, then we provide a comparison of the anomaly detection performance obtained on various metrics, to conclude with an ablation that motivates our current design choices according to prior experiments.

Unless specified otherwise, we train and evaluate all models and baselines on mask images of the tracker channel.

5.1 Metrics

For the evaluation of both baselines and our proposed models, we treat the anomalies (the two signals) as the positive class and employ two popular metrics in out-of-distribution detection [59]: the area under the receiving operating characteristic curve (AUROC), and the false positive rate at $N\%$ of the true positive rate (FPRN). The area under the ROC summarizes the performance of the discriminator across multiple thresholds, while the FPRN evaluates performance at one specific threshold value: such threshold is often specific for the application and domain requirement, in our case we choose $N\% = 40\%$ thus targeting a signal efficiency of 40%; naming the metric FPR40.

The AUROC can be considered as the probability that a signal sample is assigned a higher AD score than a background example. Thus, higher AUROC values are better, depicting a higher retention of the signal at a lower background efficiency (and so at a higher rejection rate of the background.) The FPRN metric is more suited to compare strong models, interpreted as the probability that a normal (background) sample is flagged as an anomaly (so as a signal) when the 40% of signals are correctly detected. Since we want to decrease such false alarm probability, lower FPR40 values indicate a better model.

Both metrics are evaluated at all the mediator masses for both signals, as well as providing overall performance by averaging them.

5.2 Baselines

For a fair comparison and assessment of our method, we determined some baseline discriminators: two physics-motivated ones, and a fully supervised model. The two physics discriminators are respectively based on the *total energy* (i.e. the sum of E_T deposits in each image channel), and the nTracks variable. Specifically, the nTracks is a model-independent classical variable corresponding to the total number of tracks (provided by track reconstruction algorithms) generated by an event in the detector. Such quantity is related to the number of decay products providing the best approximation of such to discern the signal particles, being also independent of the binning used to discretize the detector resolution. In particular, we define the total energy baseline as follows:

$$s^{(k)}(c) = \sum_i^H \sum_j^W x_{i,j,c}^{(k)}, \quad c \in \{0, 1, 2\} \quad (5)$$

where: $s^{(k)}(c)$ is the score value for channel c (corresponding to the tracker, ECAL, and HCAL) of the k -th image $x^{(k)}$ with height H and width W . Discrimination will be then performed according to the obtained scores, s , per channel.

Furthermore, we also considered the performance of a *supervised* model, therefore assuming an ideal setting in which we would have perfect knowledge about the data. Such a supervised baseline will provide a good approximation regarding upper-bound discrimination performance, that our unsupervised model may achieve at its best. In particular, we considered a strong model a *Compact Convolutional Transformer* (CCT) [77], that already outperformed a simpler convolutional network in our prior experiments: more details about the CCT architecture and training are available in the appendix A.3.

The performance of the baselines is summarized in both tables 4 and 5. As we can see, for the total energy baseline, each image channel has a different discrimination power. Moreover, for the SUEP signal happens that the sum of E_T deposits of the signal is actually lower than the one of the QCD background, resulting in shifted distributions of scores that yield an area of the ROC below 50%. For such baselines, it indicates that one signal (the SUEPs) is less complex than the background. Instead, such an issue does not occur for the nTracks baseline, which already provides a quite good separation performance for both signals on both evaluation metrics, especially for the SUEPs at high mass: as stated in [19], counting the number of tracks is particularly sensitive to high multiplicity soft particles like SUEPs,

Baseline	SUEP (GeV)							SVJ (TeV)			
	125	200	300	400	700	1000	mAUC	2.1	3.1	4.1	mAUC
Total energy (Trk)	45.18	48.4	54.13	58.51	67.39	70.89	57.42	55.86	72.13	81.46	69.82
Total energy (ECAL)	26.25	27.11	28.94	30.48	32.77	33.15	29.78	52.49	68.05	77.95	66.16
Total energy (HCAL)	26.22	25.38	25.77	25.98	25.21	23.74	25.38	64.46	80.17	88.15	77.59
Total energy (sum)	31.34	32.49	35.88	38.58	44.04	46.09	38.07	60.16	76.82	85.71	74.23
Number of Tracks	78.68	92.39	98.31	99.6	99.94	99.93	94.81	82.05	89.32	92.92	88.1
Supervised CCT [77]	89.72	96.58	98.88	99.42	99.87	99.93	97.4	96.05	98.17	98.76	97.66

Table 4: Baselines: AUROC metric, higher is better. mAUC denotes the mean AUROC, averaged over all the mediator masses for a given signal.

Baseline	SUEP (GeV)							SVJ (TeV)			
	125	200	300	400	700	1000	mFPR	2.1	3.1	4.1	mFPR
Total energy (Trk)	50.63	48.11	41.81	37.71	29.3	25.11	38.78	33.84	17.46	9.155	20.15
Total energy (ECAL)	72.4	70.93	69.09	66.92	64.39	64.21	67.99	37.36	20.43	11.51	23.1
Total energy (HCAL)	73.19	74.44	73.57	73.57	75.31	77.04	74.52	26.81	11.87	5.299	14.66
Total energy (sum)	66.03	65.77	61.35	58.21	52.88	50.54	59.13	30.82	14.5	6.939	17.42
Number of Tracks	11.84	2.849	0.277	0.028	~ 0	~ 0	2.5	5.45	1.599	0.539	2.53
Supervised CCT [77]	0.242	0.016	0.002	~ 0	~ 0	~ 0	0.04	0.121	0.021	0.005	0.05

Table 5: Baselines: FPR40 metric, lower is better. mFPR indicates the mean FPR40, obtained by averaging over all the mediator masses for a given signal.

making them easier to identify. Compared to the AUROC the FPR40 metric helps us better understand the shape of the ROC curve around our target signal efficiency of 40%, showing a very high (almost ideal) background rejection rate for the supervised classifier in all the benchmark scenarios.

5.3 Anomaly Detection

We have compared our two models (the CoDAE and Categorical CoDVAE) against two popular anomaly detection models: an AE inspired⁸ by [8], and the Dirichlet VAE from [21]. In particular, the Dirichlet VAE is a weakly-supervised approach that also requires a fraction of the signals for training: we assume a realistic setting in which the background is contaminated with 0.01% of the signals. The AE model has a total of 600k parameters, a latent space of size 32, and was trained to minimize a mean squared loss. Instead, for the Dirichlet VAE we normalize each training image to sum to one and use the same architecture (resulting in about 2M parameters, and three latent components) and optimizer hyperparameters as described in [21]. For both compared models, we apply our data augmentations, and use the AdamW optimizer: for the AE we use the same hyperparameters of our models. We trained both AE and Dirichlet VAE for 50 epochs (the latter converged earlier in training), the CoDAE for 30 epochs, and the Categorical CoDVAE for 100 of them since we observed slower convergence compared to the CoDAE. The batch size is 128 for all models.

For all models, we computed the anomaly scores defined in section 4.4 where possible, and evaluated their respective AUROC and FPR40. In particular, in tables 6 and 7 we provide the results for the best scores on average, while the full evaluation is available in the appendix A.5.

Compared to the nTracks baseline (table 4 and 5), which requires counting the track multiplicity possible only if fully reconstructing the event as in an off-line analysis, we are already able to get competitive performance in the latent space (figure 3) and even improve by a neat margin when using reconstruction scores such as the BCE or SSE. We can notice that for some benchmark points, like SUEP(400 GeV), SUEP(700 GeV) and SUEP(100 GeV), the AUC easily saturates (table 6) attaining an almost perfect background rejection (table 7), therefore the improvement brought by a data-driven approach is negligible. Indeed, these are easier to detect since they are expected to deviate significantly

⁸The authors provide only a figure outlining their model architecture and not a comprehensive description; we did our best to mimic their approach.

Model	SUEP (GeV)							SVJ (TeV)			
	125	200	300	400	700	1000	mAUC	2.1	3.1	4.1	mAUC
CoDAE (Z_1)	79.17	93.14	98.62	99.71	99.95	99.94	95.09	83.37	88.07	90.49	87.31
CoDAE (BCE)	86.43	96.82	99.5	99.91	99.98	99.98	97.1	85.72	89.94	92.14	89.26
Cat. CoDVAE (Z_1)	77.54	91.5	97.71	99.21	99.42	99.19	94.1	81.36	86.4	88.9	85.55
Cat. CoDVAE (KL-F)	69.32	83.92	93.18	96.38	98.04	98.18	89.84	79.69	84.08	86.11	83.3
Cat. CoDVAE (SSE)	86.93	97.01	99.51	99.9	99.98	99.98	97.22	85.29	89.78	92.04	89.04
AE [8]-like	83.89	94.6	98.69	99.68	99.95	99.94	96.13	83.26	88.72	91.44	87.81
Dirichlet VAE [21]	51.93	54.99	59.58	63.17	71.16	74.51	62.55	63.52	67.37	69.26	66.72

Table 6: Comparison of anomaly detection models on test-set. AUROC metric, higher is better. For the AE we use the PixelSum score, and the second latent component (Z_2) for the Dirichlet VAE.

Model	SUEP (GeV)							SVJ (TeV)			
	125	200	300	400	700	1000	mFPR	2.1	3.1	4.1	mFPR
CoDAE (Z_1)	11.95	2.535	0.228	0.022	0.001	0.001	2.46	4.541	1.988	1.144	2.56
CoDAE (BCE)	7.292	1.108	0.078	0.004	~ 0	~ 0	1.41	3.047	1.214	0.636	1.63
Cat. CoDVAE (Z_1)	12.91	3.329	0.575	0.219	0.227	0.341	2.93	5.9	2.866	1.85	3.54
Cat. CoDVAE (KL-F)	19.08	7.498	2.635	1.452	0.739	0.677	5.35	7.425	4.913	4.085	5.47
Cat. CoDVAE (SSE)	6.652	0.944	0.071	0.007	~ 0	~ 0	1.28	3.065	1.176	0.588	1.61
AE [8]-like	8.22	1.904	0.211	0.035	~ 0	~ 0	1.73	4.346	1.74	0.863	2.32
Dirichlet VAE [21]	26.06	17.38	10.15	6.66	2.572	1.42	10.71	21.42	14.89	10.92	15.74

Table 7: Comparison of anomaly detection models on test-set. FPR40 metric, lower is better.

from the QCD background. Instead, in the most challenging scenarios our models achieve an AUC improvement of at most +8% for SUEPs and +3% for SVJs, as well as a reduction of FPR of at most 5% for SUEPs and 2% for SVJs, at the predefined signal efficiency compared to the nTracks baseline. Our models are able to reduce the gap with the supervised classifier despite being trained on the background class only.

5.4 Reconstruction Quality

To assess the reconstruction quality of the compared models, we evaluate two metrics: the mean squared error (MSE), and the structural similarity (SSIM) index [72]. In particular, the popular MSE metric is useful for determining the texture quality of the reconstructions, since it looks at pixel-level differences. Instead, the SSIM is a perceptual quality metric designed to better match the perceived visual quality of humans. These two metrics are complementary since the MSE looks at fine details while the SSIM at the global appearance of the images, providing a more comprehensive assessment of the quality of the reconstructed samples.

Metric	CoDAE	CoDVAE	AE [8]	Dirichlet VAE [21]
MSE	12.14 (± 9.1)	17.72 (± 12.98)	70.88 (± 24.74)	79.29 (± 26.1)
SSIM	0.97 (± 0.03)	0.95 (± 0.04)	0.36 (± 0.12)	0.17 (± 0.11)

Table 8: Evaluation of reconstruction quality: QCD test images. Lower values of MSE as well higher SSIM ones are considered to be better. Each entry denotes the average metric value as well as its standard deviation (in parenthesis.) By design the Dirichlet VAE outputs images that sum to one, so we undo normalization before computing the metrics.

Reconstruction performance is summarized in table 8 as well visually in figure 4. From both we can deduce that our two models achieve the lowest MSE and highest structural similarity, attaining accurate single-sample reconstructions resulting in good predictions on average. As we can notice from table 8, all models show some variance in the reconstructed background, indicating that some QCD samples deviate from the ideal background event. Moreover,

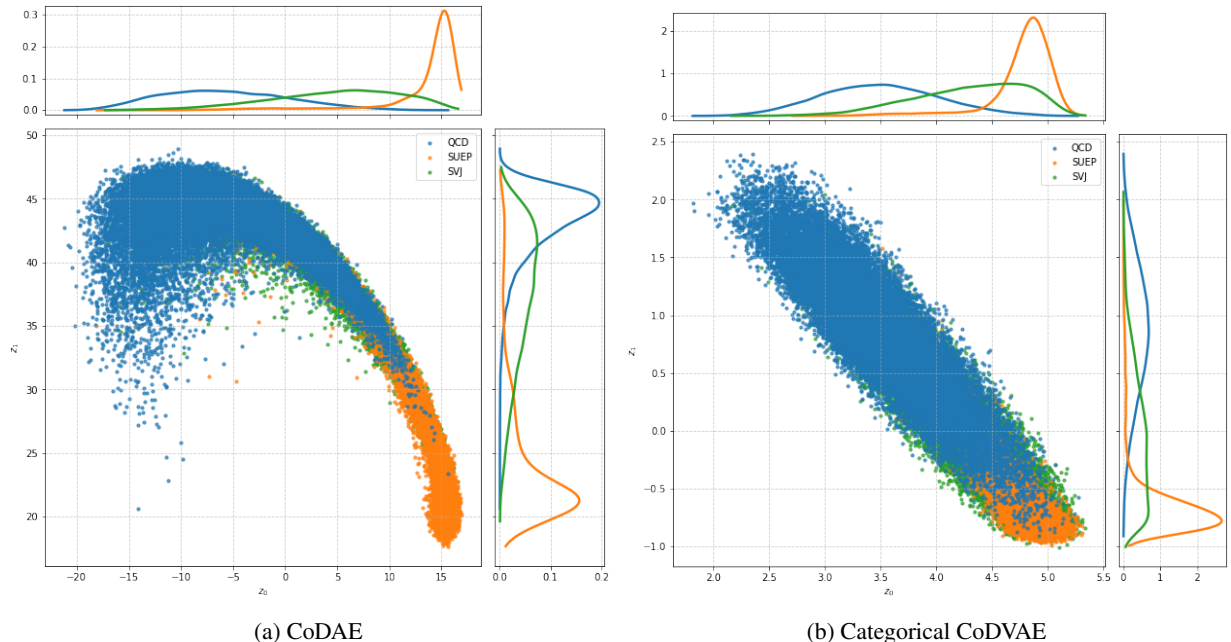


Figure 3: The auxiliary latent space $Z_{m,s}$, learned by our two models along with density estimates of their two components. As we can see, QCD and SUEPs look well separated, instead the SVJs span in between the two classes.

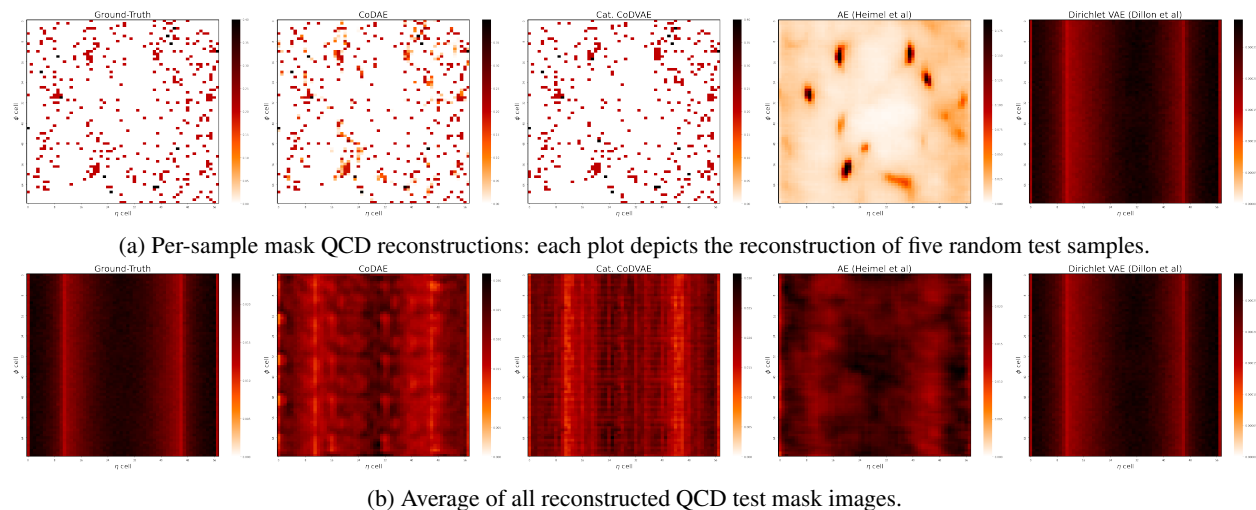


Figure 4: Comparison of per-sample (first row) and average (second row) reconstructions. In order: ground-truth, CoDAE, Categorical CoDAE, AE [8], and Dirichlet VAE [21]. As we can see our two models (second and third columns) are capable of pixel-accurate single-sample reconstructions, whereas the AE only captures the prominent pixels, and the Dirichlet VAE learns to predict a sort of average image instead.

AE-based models show softer and smoother pixel predictions whereas the Categorical CoDVAE, thanks to its Bernoulli decoder, is capable of sharp reconstructions by taking the mode of each learned distribution, one per output pixel. Furthermore, from the figure 4 we can observe how the Dirichlet VAE, which is designed to capture a multi-modal latent space distribution, only captures the “QCD mode” since each sample being either background or signal is predicted as being a sort of average of QCD images: this is confirmed by the low reconstruction metrics. We noticed similar behavior in our prior experiments when training regular AEs with a small latent space (e.g. 2), even with a high-capacity residual encoder.

We want to highlight the importance of accurate (or at least coherent) reconstructions. Since anomaly detection scores can be defined from such predictions, it is necessary to avoid the model learning to predict some spurious pattern or

artifact instead of the inputs, otherwise, it would be difficult to understand for a human why a new sample deviates from the training data. This is essential to obtain coherent anomaly detection predictions, to have a trustworthy model, and even to debug the model itself once deployed.

5.5 Ablations and Prior Experiments

In this section, we motivate the design choices of our models determined by prior experiments. In particular, we discuss their impact on both anomaly detection and reconstruction quality:

- **2d latent space:** in our early experiments we tested a regular AE design, whose encoder and decoder were implemented as shallow convolutional networks. We discovered that even with large latent space vectors, the model struggled to reconstruct with fidelity the samples. Moreover, when constraining Z to have two components, i.e. $|Z| = 2$, the decoder predicted only artifacts that we noticed to be weakly correlated with the location of the brightest pixels: although the 2d latent space provided an almost satisfying separation of the two signals. *This hints us the need for higher capacity and deeper networks for accurate reconstructions.*
- **Residual networks:** implementing both the encoder and decoder networks as ResNet-like [62], provided enough capacity to recover some fine detail even when $|Z| = 2$. However, the artifacts were still present in the reconstructed images, although being more localized in the bottom part. The most striking finding was that the 2d latents were not informative at all, attaining around 60% AUROC at most, on average. *This suggested to us that a residual encoder was not suitable to capture a discriminative 2d bottleneck.*
- **Dual encoders:** to confirm the previous finding, we introduced a dual-encoder design. We evaluated different combinations of them, being both residual or convolutional, and mixed as well. The winning combination was to have two encoders: one residual intended for reconstruction quality, and a convolutional one (thus shallower) to capture an informative bottleneck. In our experiments, both networks encoded the input image to the same latent space dimensionality, thus having two of them Z_1 and Z_2 : where $|Z_1| = |Z_2| = 2$. We discovered that a learned *linear projection* of both achieved the best AD performance, although the reconstructions were not improving at all. The role of projection was to combine the information encoded from both energy (I) and mask images (I_m): I was fed to the residual encoder, and I_m to the convolutional one; also this choice was validated during the early experimentation. At this point, we discovered two things: *information learned from I_m enhanced the encoding of I through the projection, but the latent space size was too small to enable high-quality reconstructions.*
- **Conditioning:** to achieve the best of both worlds, we decided to learn two separate latent spaces. A high capacity convolutional bottleneck (that we called Z), as suggested by [63], to capture fine details, and a 2d one (Z_m) to learn discriminative information. Since these two spaces have both different sizes and dimensionality, a projection was not possible, and so we opted for a form of conditioning [70] that also promoted learning disentangled representations [71]. *Doing so allowed to also learn the second encoder, while achieving high reconstruction faithfulness as well as a discriminative auxiliary latent space.*
- **Mask image:** the previous experiments were conducted by training the AE models to reconstruct the energy images, either with *one* channel (i.e. obtained by summing over tracker, ECAL, and HCAL pixels) or *three* channels. The reconstruction results were similar, and also the discrimination power of the auxiliary Z_m that, although good, was not enough to surpass the nTracks baseline. So we considered two facts: 1) that the mask image is related to the nTracks variable being an approximation of the reconstructed tracks, and 2) that such baseline is much more discriminative than the total energy. Therefore, we retrained our conditional dual-AE on mask images (I_m) instead of energy deposits ones, also discarding the ECAL and HCAL channels as we wanted to consider only information from the tracker, and discovered that: Z_m was more informative approaching the performance of the nTracks baseline, and that the reconstruction scores were much more discriminative without the calorimeter information.

In our case, the information brought by the calorimeter (ECAL and HCAL channels) was not useful causing instead a negative effect on the class separation power of the model: one explanation for SUEPs can be related to the sphericity of the events, lacking hard and isolated objects thus resembling pile-up at the calorimeter level [19]. We expect ECAL and HCAL information to be still useful in general, especially for searching long-lived particles.

6 Conclusions

We demonstrated the first successful application of (variational) auto-encoders to be deployed in the trigger stages of experiments like ATLAS and CMS to search for two dark showers models: the soft unclustered energy patterns

and semi-visible jets. We framed the problem as anomaly detection assuming having access to a normal-only set of samples, corresponding to the QCD background. Unlike the common trend in many related works, we do not employ a specific particle-based pre-processing of our data, nor low- or high-level features, but instead learn directly from raw images of particle collisions obtained by discretizing the detector response, thus reducing the dependency on the physics model: making our approach very general, thus suitable for a wide range of applications in new physics scenarios. We proposed a dual-encoder design which, by means of conditioning, is able to learn, without supervision, an auxiliary latent space compact enough to be both visualized and directly usable as scores for anomaly detection. Such a small encoder is more suitable than a full AE model for deployment on the target platform with limited time budgets. Finally, we compared our models against popular anomaly detection methods in physics and as well competitive baselines, achieving superior performance and background rejection rates, thus reducing the gap to a fully supervised, albeit strongly model-dependent classifier.

Acknowledgements

L. Anzalone is supported by the University of Bologna, Italy. S. S. Chhibra, B. Maier and N. Chernyavskaya are supported by CERN, Switzerland under the Senior Research Fellowship Programme. S. S. Chhibra is partly supported by QMUL, UK. B. Maier is partly supported by KIT, Germany. M. Pierini is supported by the European Research Council (ERC) under the European Union’s Horizon 2020 research and innovation program (Grant Agreement No. 772369).

References

- [1] S. Chatrchyan *et al.*, “Observation of a New Boson at a Mass of 125 GeV with the CMS Experiment at the LHC,” *Phys. Lett. B*, vol. 716, pp. 30–61, 2012.
- [2] P. Baldi, P. Sadowski, and D. Whiteson, “Searching for Exotic Particles in High-Energy Physics with Deep Learning,” *Nature Commun.*, vol. 5, p. 4308, 2014.
- [3] L. Anzalone, T. Diotallevi, and D. Bonacorsi, “Improving parametric neural networks for high-energy physics (and beyond),” *Machine Learning: Science and Technology*, vol. 3, p. 035017, oct 2022.
- [4] A. Butter *et al.*, “The Machine Learning landscape of top taggers,” *SciPost Phys.*, vol. 7, p. 014, 2019.
- [5] G. Cowan, K. Cranmer, E. Gross, and O. Vitells, “Asymptotic formulae for likelihood-based tests of new physics,” *Eur. Phys. J. C*, vol. 71, p. 1554, 2011. [Erratum: *Eur.Phys.J.C* 73, 2501 (2013)].
- [6] D. P. Kingma and M. Welling, “Auto-encoding variational bayes,” in *2nd International Conference on Learning Representations, ICLR 2014, Banff, AB, Canada, April 14-16, 2014, Conference Track Proceedings* (Y. Bengio and Y. LeCun, eds.), 2014.
- [7] J. Masci, U. Meier, D. C. Ciresan, and J. Schmidhuber, “Stacked convolutional auto-encoders for hierarchical feature extraction,” in *Artificial Neural Networks and Machine Learning - ICANN 2011 - 21st International Conference on Artificial Neural Networks, Espoo, Finland, June 14-17, 2011, Proceedings, Part I* (T. Honkela, W. Duch, M. A. Girolami, and S. Kaski, eds.), vol. 6791 of *Lecture Notes in Computer Science*, pp. 52–59, Springer, 2011.
- [8] T. Heimel, G. Kasieczka, T. Plehn, and J. M. Thompson, “QCD or What?,” *SciPost Phys.*, vol. 6, no. 3, p. 030, 2019.
- [9] T. Cheng, J.-F. Arguin, J. Leissner-Martin, J. Pilette, and T. Golling, “Variational autoencoders for anomalous jet tagging,” *Phys. Rev. D*, vol. 107, no. 1, p. 016002, 2023.
- [10] F. Canelli, A. de Cosa, L. L. Pottier, J. Niedziela, K. Pedro, and M. Pierini, “Autoencoders for semivisible jet detection,” *JHEP*, vol. 02, p. 074, 2022.
- [11] T. Finke, M. Krämer, A. Morandini, A. Mück, and I. Oleksiyuk, “Autoencoders for unsupervised anomaly detection in high energy physics,” *JHEP*, vol. 06, p. 161, 2021.
- [12] B. M. Dillon, L. Favaro, T. Plehn, P. Sorrenson, and M. Krämer, “A Normalized Autoencoder for LHC Triggers,” 6 2022.
- [13] B. Bortolato, A. Smolkovič, B. M. Dillon, and J. F. Kamenik, “Bump hunting in latent space,” *Phys. Rev. D*, vol. 105, no. 11, p. 115009, 2022.
- [14] J. Barron, D. Curtin, G. Kasieczka, T. Plehn, and A. Spourdalakis, “Unsupervised hadronic SUEP at the LHC,” *JHEP*, vol. 12, p. 129, 2021.

- [15] M. J. Strassler and K. M. Zurek, “Echoes of a hidden valley at hadron colliders,” *Phys. Lett. B*, vol. 651, pp. 374–379, 2007.
- [16] T. Cohen, M. Lisanti, and H. K. Lou, “Semivisible Jets: Dark Matter Undercover at the LHC,” *Phys. Rev. Lett.*, vol. 115, no. 17, p. 171804, 2015.
- [17] T. Cohen, M. Lisanti, H. K. Lou, and S. Mishra-Sharma, “LHC Searches for Dark Sector Showers,” *JHEP*, vol. 11, p. 196, 2017.
- [18] D. Kar and S. Sinha, “Exploring jet substructure in semi-visible jets,” *SciPost Phys.*, vol. 10, no. 4, p. 084, 2021.
- [19] S. Knapen, S. Pagan Griso, M. Papucci, and D. J. Robinson, “Triggering Soft Bombs at the LHC,” *JHEP*, vol. 08, p. 076, 2017.
- [20] V. Khachatryan *et al.*, “The CMS trigger system,” *JINST*, vol. 12, no. 01, p. P01020, 2017.
- [21] B. M. Dillon, T. Plehn, C. Sauer, and P. Sorrenson, “Better Latent Spaces for Better Autoencoders,” *SciPost Phys.*, vol. 11, p. 061, 2021.
- [22] G. Kasieczka, R. Mastandrea, V. Mikuni, B. Nachman, M. Pettee, and D. Shih, “Anomaly detection under coordinate transformations,” *Phys. Rev. D*, vol. 107, no. 1, p. 015009, 2023.
- [23] “LHC Machine,” *JINST*, vol. 3, p. S08001, 2008.
- [24] T. R. A. Denk, “Quirky composite dark matter,” bachelor thesis, Tech. U., Munich, 2011.
- [25] S. Born, R. Karur, S. Knapen, and J. Shelton, “Scouting for dark showers at CMS and LHCb,” 3 2023.
- [26] A. Collaboration, G. Aad, E. Abat, J. Abdallah, A. Abdelalim, A. Abdesselam, O. Abidinov, B. Abi, M. Abolins, H. Abramowicz, *et al.*, “The atlas experiment at the cern large hadron collider,” 2008.
- [27] S. Chatrchyan *et al.*, “The CMS Experiment at the CERN LHC,” *JINST*, vol. 3, p. S08004, 2008.
- [28] “The CMS tracker: addendum to the Technical Design Report,” 2000.
- [29] C. Biino, “The cms electromagnetic calorimeter: overview, lessons learned during run 1 and future projections,” in *Journal of Physics: Conference Series*, vol. 587, p. 012001, IOP Publishing, 2015.
- [30] “The CMS hadron calorimeter project: Technical Design Report,” 1997.
- [31] J. de Favereau, C. Delaere, P. Demin, A. Giammanco, V. Lemaitre, A. Mertens, and M. Selvaggi, “Delphes 3: a modular framework for fast simulation of a generic collider experiment,” *JHEP*, vol. 2014, p. 57, 2014.
- [32] T. Sjöstrand, S. Ask, J. R. Christiansen, R. Corke, N. Desai, P. Ilten, S. Mrenna, S. Prestel, C. O. Rasmussen, and P. Z. Skands, “An introduction to PYTHIA 8.2,” *Comp. Phys. Comm.*, vol. 191, pp. 159 – 177, 2015.
- [33] R. Corke and T. Sjostrand, “Interleaved Parton Showers and Tuning Prospects,” *JHEP*, vol. 03, p. 032, 2011.
- [34] G. E. Hinton and R. R. Salakhutdinov, “Reducing the dimensionality of data with neural networks,” *science*, vol. 313, no. 5786, pp. 504–507, 2006.
- [35] P. Vincent, H. Larochelle, I. Lajoie, Y. Bengio, and P. Manzagol, “Stacked denoising autoencoders: Learning useful representations in a deep network with a local denoising criterion,” *J. Mach. Learn. Res.*, vol. 11, pp. 3371–3408, 2010.
- [36] D. Bank, N. Koenigstein, and R. Giryes, “Autoencoders,” *arXiv preprint arXiv:2003.05991*, 2020.
- [37] C. P. Burgess, I. Higgins, A. Pal, L. Matthey, N. Watters, G. Desjardins, and A. Lerchner, “Understanding disentangling in β -vae,” *CoRR*, vol. abs/1804.03599, 2018.
- [38] E. Jang, S. Gu, and B. Poole, “Categorical reparameterization with gumbel-softmax,” in *5th International Conference on Learning Representations, ICLR 2017, Toulon, France, April 24-26, 2017, Conference Track Proceedings*, OpenReview.net, 2017.
- [39] C. J. Maddison, A. Mnih, and Y. W. Teh, “The concrete distribution: A continuous relaxation of discrete random variables,” in *5th International Conference on Learning Representations, ICLR 2017, Toulon, France, April 24-26, 2017, Conference Track Proceedings*, OpenReview.net, 2017.
- [40] I. A. M. Huijben, W. Kool, M. B. Paulus, and R. J. G. van Sloun, “A review of the gumbel-max trick and its extensions for discrete stochasticity in machine learning,” *IEEE Trans. Pattern Anal. Mach. Intell.*, vol. 45, no. 2, pp. 1353–1371, 2023.
- [41] A. Abid, M. F. Balin, and J. Y. Zou, “Concrete autoencoders for differentiable feature selection and reconstruction,” *CoRR*, vol. abs/1901.09346, 2019.

- [42] S. Havrylov and I. Titov, “Emergence of language with multi-agent games: Learning to communicate with sequences of symbols,” in *Advances in Neural Information Processing Systems 30: Annual Conference on Neural Information Processing Systems 2017, December 4-9, 2017, Long Beach, CA, USA* (I. Guyon, U. von Luxburg, S. Bengio, H. M. Wallach, R. Fergus, S. V. N. Vishwanathan, and R. Garnett, eds.), pp. 2149–2159, 2017.
- [43] S. Yan, J. S. Smith, W. Lu, and B. Zhang, “Hierarchical multi-scale attention networks for action recognition,” *Signal Process. Image Commun.*, vol. 61, pp. 73–84, 2018.
- [44] K. Sohn, H. Lee, and X. Yan, “Learning structured output representation using deep conditional generative models,” in *Advances in Neural Information Processing Systems 28: Annual Conference on Neural Information Processing Systems 2015, December 7-12, 2015, Montreal, Quebec, Canada* (C. Cortes, N. D. Lawrence, D. D. Lee, M. Sugiyama, and R. Garnett, eds.), pp. 3483–3491, 2015.
- [45] N. Dilokthanakul, P. A. M. Mediano, M. Garnelo, M. C. H. Lee, H. Salimbeni, K. Arulkumaran, and M. Shanahan, “Deep unsupervised clustering with gaussian mixture variational autoencoders,” *CoRR*, vol. abs/1611.02648, 2016.
- [46] E. Dupont, “Learning disentangled joint continuous and discrete representations,” in *Advances in Neural Information Processing Systems 31: Annual Conference on Neural Information Processing Systems 2018, NeurIPS 2018, December 3-8, 2018, Montréal, Canada* (S. Bengio, H. M. Wallach, H. Larochelle, K. Grauman, N. Cesa-Bianchi, and R. Garnett, eds.), pp. 708–718, 2018.
- [47] R. Chalapathy and S. Chawla, “Deep learning for anomaly detection: A survey,” *CoRR*, vol. abs/1901.03407, 2019.
- [48] K. Fraser, S. Homiller, R. K. Mishra, B. Ostdiek, and M. D. Schwartz, “Challenges for unsupervised anomaly detection in particle physics,” *JHEP*, vol. 03, p. 066, 2022.
- [49] B. Schölkopf, R. C. Williamson, A. J. Smola, J. Shawe-Taylor, and J. C. Platt, “Support vector method for novelty detection,” in *Advances in Neural Information Processing Systems 12, [NIPS Conference, Denver, Colorado, USA, November 29 - December 4, 1999]* (S. A. Solla, T. K. Leen, and K. Müller, eds.), pp. 582–588, The MIT Press, 1999.
- [50] F. T. Liu, K. M. Ting, and Z. Zhou, “Isolation-based anomaly detection,” *ACM Trans. Knowl. Discov. Data*, vol. 6, no. 1, pp. 3:1–3:39, 2012.
- [51] T. Schlegl, P. Seeböck, S. M. Waldstein, U. Schmidt-Erfurth, and G. Langs, “Unsupervised anomaly detection with generative adversarial networks to guide marker discovery,” in *Information Processing in Medical Imaging - 25th International Conference, IPMI 2017, Boone, NC, USA, June 25-30, 2017, Proceedings* (M. Niethammer, M. Styner, S. R. Aylward, H. Zhu, I. Oguz, P. Yap, and D. Shen, eds.), vol. 10265 of *Lecture Notes in Computer Science*, pp. 146–157, Springer, 2017.
- [52] S. Yoon, Y. Noh, and F. C. Park, “Autoencoding under normalization constraints,” in *Proceedings of the 38th International Conference on Machine Learning, ICML 2021, 18-24 July 2021, Virtual Event* (M. Meila and T. Zhang, eds.), vol. 139 of *Proceedings of Machine Learning Research*, pp. 12087–12097, PMLR, 2021.
- [53] W. Joo, W. Lee, S. Park, and I. Moon, “Dirichlet variational autoencoder,” *Pattern Recognit.*, vol. 107, p. 107514, 2020.
- [54] B. M. Dillon, R. Mastandrea, and B. Nachman, “Self-supervised anomaly detection for new physics,” *Phys. Rev. D*, vol. 106, no. 5, p. 056005, 2022.
- [55] A. Vaswani, N. Shazeer, N. Parmar, J. Uszkoreit, L. Jones, A. N. Gomez, L. Kaiser, and I. Polosukhin, “Attention is all you need,” in *Advances in Neural Information Processing Systems 30: Annual Conference on Neural Information Processing Systems 2017, December 4-9, 2017, Long Beach, CA, USA* (I. Guyon, U. von Luxburg, S. Bengio, H. M. Wallach, R. Fergus, S. V. N. Vishwanathan, and R. Garnett, eds.), pp. 5998–6008, 2017.
- [56] B. M. Dillon, G. Kasieczka, H. Olschlager, T. Plehn, P. Sorrenson, and L. Vogel, “Symmetries, safety, and self-supervision,” *SciPost Phys.*, vol. 12, no. 6, p. 188, 2022.
- [57] E. M. Metodiev, B. Nachman, and J. Thaler, “Classification without labels: Learning from mixed samples in high energy physics,” *Journal of High Energy Physics*, vol. 2017, no. 10, pp. 1–18, 2017.
- [58] E. Govorkova *et al.*, “Autoencoders on field-programmable gate arrays for real-time, unsupervised new physics detection at 40 MHz at the Large Hadron Collider,” *Nature Mach. Intell.*, vol. 4, pp. 154–161, 2022.
- [59] D. Hendrycks, M. Mazeika, and T. G. Dietterich, “Deep anomaly detection with outlier exposure,” in *7th International Conference on Learning Representations, ICLR 2019, New Orleans, LA, USA, May 6-9, 2019*, OpenReview.net, 2019.
- [60] G. Kasieczka and D. Shih, “Robust Jet Classifiers through Distance Correlation,” *Phys. Rev. Lett.*, vol. 125, no. 12, p. 122001, 2020.

- [61] G. Kasieczka, B. Nachman, M. D. Schwartz, and D. Shih, “Automating the ABCD method with machine learning,” *Phys. Rev. D*, vol. 103, no. 3, p. 035021, 2021.
- [62] K. He, X. Zhang, S. Ren, and J. Sun, “Deep residual learning for image recognition,” in *2016 IEEE Conference on Computer Vision and Pattern Recognition, CVPR 2016, Las Vegas, NV, USA, June 27-30, 2016*, pp. 770–778, IEEE Computer Society, 2016.
- [63] I. Manakov, M. Rohm, and V. Tresp, “Walking the tightrope: An investigation of the convolutional autoencoder bottleneck,” *CoRR*, vol. abs/1911.07460, 2019.
- [64] D. Ulyanov, A. Vedaldi, and V. S. Lempitsky, “Instance normalization: The missing ingredient for fast stylization,” *CoRR*, vol. abs/1607.08022, 2016.
- [65] S. Ioffe and C. Szegedy, “Batch normalization: Accelerating deep network training by reducing internal covariate shift,” in *Proceedings of the 32nd International Conference on Machine Learning, ICML 2015, Lille, France, 6-11 July 2015* (F. R. Bach and D. M. Blei, eds.), vol. 37 of *JMLR Workshop and Conference Proceedings*, pp. 448–456, JMLR.org, 2015.
- [66] A. Krizhevsky, I. Sutskever, and G. E. Hinton, “Imagenet classification with deep convolutional neural networks,” *Commun. ACM*, vol. 60, no. 6, pp. 84–90, 2017.
- [67] S. Xie, R. B. Girshick, P. Dollár, Z. Tu, and K. He, “Aggregated residual transformations for deep neural networks,” in *2017 IEEE Conference on Computer Vision and Pattern Recognition, CVPR 2017, Honolulu, HI, USA, July 21-26, 2017*, pp. 5987–5995, IEEE Computer Society, 2017.
- [68] A. L. Maas, A. Y. Hannun, A. Y. Ng, *et al.*, “Rectifier nonlinearities improve neural network acoustic models,” in *Proc. icml*, vol. 30, p. 3, Atlanta, Georgia, USA, 2013.
- [69] M. Lin, Q. Chen, and S. Yan, “Network in network,” in *2nd International Conference on Learning Representations, ICLR 2014, Banff, AB, Canada, April 14-16, 2014, Conference Track Proceedings* (Y. Bengio and Y. LeCun, eds.), 2014.
- [70] V. Dumoulin, E. Perez, N. Schucher, F. Strub, H. d. Vries, A. Courville, and Y. Bengio, “Feature-wise transformations,” *Distill*, 2018. <https://distill.pub/2018/feature-wise-transformations>.
- [71] N. Watters, L. Matthey, C. P. Burgess, and A. Lerchner, “Spatial broadcast decoder: A simple architecture for learning disentangled representations in vaes,” *CoRR*, vol. abs/1901.07017, 2019.
- [72] Z. Wang, A. C. Bovik, H. R. Sheikh, and E. P. Simoncelli, “Image quality assessment: from error visibility to structural similarity,” *IEEE Trans. Image Process.*, vol. 13, no. 4, pp. 600–612, 2004.
- [73] D. P. Kingma and J. Ba, “Adam: A method for stochastic optimization,” in *3rd International Conference on Learning Representations, ICLR 2015, San Diego, CA, USA, May 7-9, 2015, Conference Track Proceedings* (Y. Bengio and Y. LeCun, eds.), 2015.
- [74] I. Loshchilov and F. Hutter, “Decoupled weight decay regularization,” in *7th International Conference on Learning Representations, ICLR 2019, New Orleans, LA, USA, May 6-9, 2019*, OpenReview.net, 2019.
- [75] K. He, X. Zhang, S. Ren, and J. Sun, “Delving deep into rectifiers: Surpassing human-level performance on imagenet classification,” in *2015 IEEE International Conference on Computer Vision, ICCV 2015, Santiago, Chile, December 7-13, 2015*, pp. 1026–1034, IEEE Computer Society, 2015.
- [76] R. Deng, C. Shen, S. Liu, H. Wang, and X. Liu, “Learning to predict crisp boundaries,” in *Proceedings of the European Conference on Computer Vision (ECCV)*, pp. 562–578, 2018.
- [77] A. Hassani, S. Walton, N. Shah, A. Abuduweili, J. Li, and H. Shi, “Escaping the big data paradigm with compact transformers,” *CoRR*, vol. abs/2104.05704, 2021.
- [78] T. Sjöstrand, S. Ask, J. R. Christiansen, R. Corke, N. Desai, P. Ilten, S. Mrenna, S. Prestel, C. O. Rasmussen, and P. Z. Skands, “An introduction to PYTHIA 8.2,” *Comput. Phys. Commun.*, vol. 191, pp. 159–177, 2015.
- [79] J. de Favereau, C. Delaere, P. Demin, A. Giammanco, V. Lemaître, A. Mertens, and M. Selvaggi, “DELPHES 3, A modular framework for fast simulation of a generic collider experiment,” *JHEP*, vol. 02, p. 057, 2014.
- [80] A. Tumasyan *et al.*, “Search for resonant production of strongly coupled dark matter in proton-proton collisions at 13 TeV,” *JHEP*, vol. 06, p. 156, 2022.
- [81] S. Knapen, J. Shelton, and D. Xu, “Perturbative benchmark models for a dark shower search program,” *Phys. Rev. D*, vol. 103, no. 11, p. 115013, 2021.
- [82] V. Nair and G. E. Hinton, “Rectified linear units improve restricted boltzmann machines,” in *Proceedings of the 27th International Conference on Machine Learning (ICML-10), June 21-24, 2010, Haifa, Israel* (J. Fürnkranz and T. Joachims, eds.), pp. 807–814, Omnipress, 2010.

- [83] L. J. Ba, J. R. Kiros, and G. E. Hinton, “Layer normalization,” *CoRR*, vol. abs/1607.06450, 2016.
- [84] D. Hendrycks and K. Gimpel, “Bridging nonlinearities and stochastic regularizers with gaussian error linear units,” *CoRR*, vol. abs/1606.08415, 2016.
- [85] G. Huang, Y. Sun, Z. Liu, D. Sedra, and K. Q. Weinberger, “Deep networks with stochastic depth,” in *Computer Vision - ECCV 2016 - 14th European Conference, Amsterdam, The Netherlands, October 11-14, 2016, Proceedings, Part IV* (B. Leibe, J. Matas, N. Sebe, and M. Welling, eds.), vol. 9908 of *Lecture Notes in Computer Science*, pp. 646–661, Springer, 2016.
- [86] V. Dumoulin and F. Visin, “A guide to convolution arithmetic for deep learning,” *CoRR*, vol. abs/1603.07285, 2016.

A Appendix

A.1 Data Generation, Simulation, and Reconstruction

Multi-jet QCD, as well as SVJ and SUEP events, are generated using PYTHIA 8.244 [78] and simulated and reconstructed with DELPHES 3.5 [79] using the CMS detector configuration. Proton-proton collisions at the LHC Run-3 centre-of-mass energy of 13.6 TeV are considered, with approximately 50 collisions per bunch crossing (pileup). A pileup reduction is applied to the reconstructed tracks: the E_T deposits in the inner tracker by the pileup tracks are removed. No pileup reduction is applied for calorimeters, as per the HLT system’s configuration during Run 3 [20].

The model parameters for the QCD events generation are identical as in [80]. For SUEP event generation, we used the SUEP_Generator plugin [81], and the following parameter settings have been used [19]:

- Mediator masses (m_H) = {125, 200, 300, 400, 700, 1000} GeV
- Dark meson mass (m_{ϕ_D}) = 2 GeV
- Branching ratio of $\phi_D \rightarrow 2Z_D = 100\%$
- Dark photon mass (m_{Z_D}) = 0.7 GeV
- Branching ratios of $Z_D \rightarrow \pi^+\pi^-, e^+e^-, \mu^+\mu^- = 70\%, 15\%, 15\%$
- Dark temperature (T_D) = 2 GeV.

The model parameters for the SVJ signal are identical to those in [10]. The mediator mass values of 2.1 TeV, 3.1 TeV, and 4.1 TeV are considered.

A.2 Event Preselection

A preselection criterion is applied to both QCD and SUEP events based on the detector’s geometry and typical characteristics of QCD events. The $|\eta|$ of E_T deposits is required to be less than 2.5, defined by the inner tracker coverage. The scalar sum of E_T of reconstructed electrons, muons, photons, and jets (denoted as H_T) in an event is required to be > 500 GeV, which is a typical H_T requirement at the HLT after L1 trigger selection during Run 3. The event preselection efficiency is found to be $\sim 85\%$ for QCD and $\sim 2.1\%$, $\sim 4.0\%$, $\sim 7.1\%$, $\sim 10.4\%$, $\sim 18.4\%$, and $\sim 22.7\%$ for SUEP(125 GeV), SUEP(200 GeV), SUEP(300 GeV), SUEP(400 GeV), SUEP(700 GeV), and SUEP(1000 GeV), respectively. The preselection efficiencies for SVJ(2.1 TeV), SVJ(3.1 TeV), and SVJ(4.1 TeV) are $\sim 9.3\%$, $\sim 9.8\%$, and $\sim 9.9\%$, respectively.

The plots showing the E_T deposits for a QCD event, a SUEP(400 GeV) event, and a SVJ(3.1 TeV) event, which satisfies the preselection criterion, in the inner tracker, ECAL, and HCAL are given in Figures 5, 6, and 7 respectively. The ECAL is 25 times more granular ($0.0174 \times 0.0174 \text{ rad}^2$ in η - ϕ) than the HCAL ($0.087 \times 0.087 \text{ rad}^2$ in η - ϕ). Hence, each HCAL pixel is divided into 25 equal pixels to match the ECAL granularity. The final shape of the images is $286 \times 360 \times 3$. For this particular QCD event, we can appreciate the typical signature of two jets in the η - ϕ plane. On the other hand, for the SUEP(400 GeV) event, there is a clear spherically-symmetric signature of a large number of low- E_T particles in ϕ .

A.3 Architecture of Supervised Baseline

The architecture of the Compact Convolutional Transformer (CCT) [77] we employ as a fully supervised model, is the following:

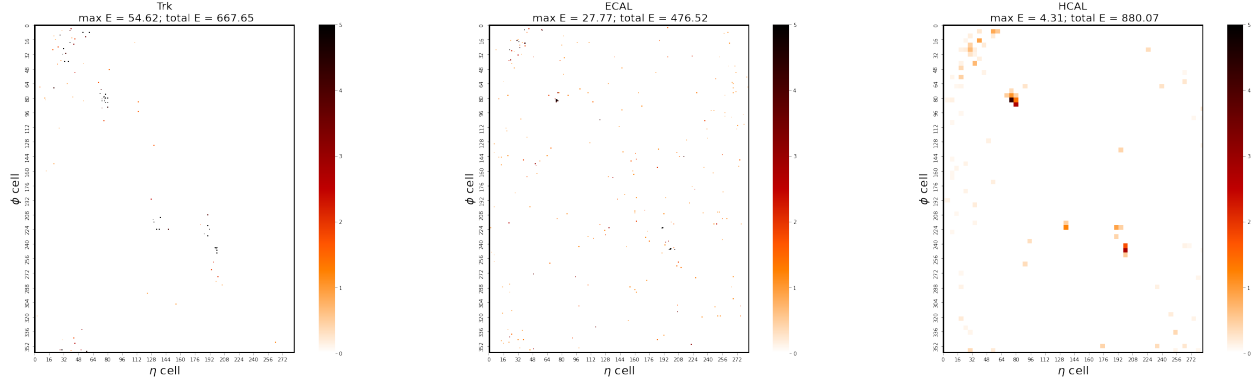


Figure 5: E_T deposits for a QCD event in the inner tracker (left), ECAL (middle), and HCAL (right). To improve the visualization of the energy deposits, the intensity of each pixel has been limited to a maximum value of five. The same is done for the next two figures. "max E " denotes the intensity of the brightest pixel, while "total E " is the sum of all pixel values.

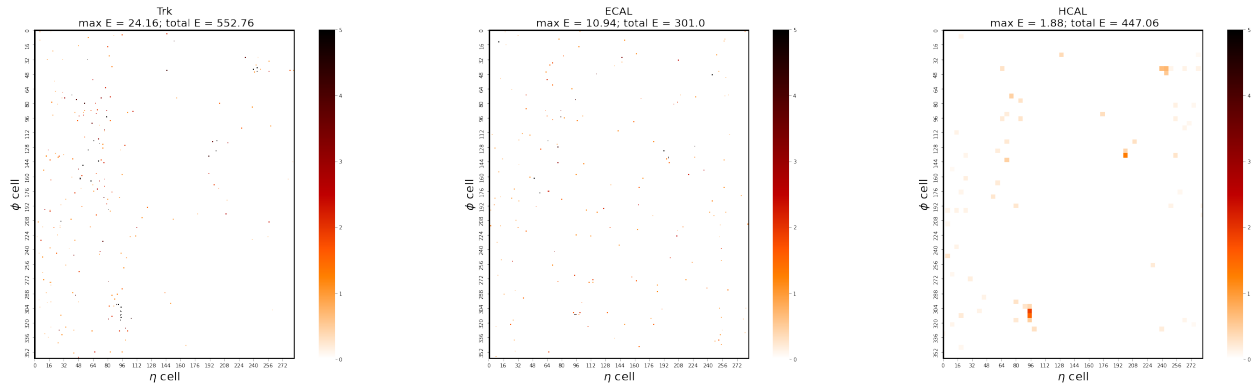


Figure 6: E_T deposits for a SUEP(400 GeV) event in the inner tracker (left), ECAL (middle), and HCAL (right).

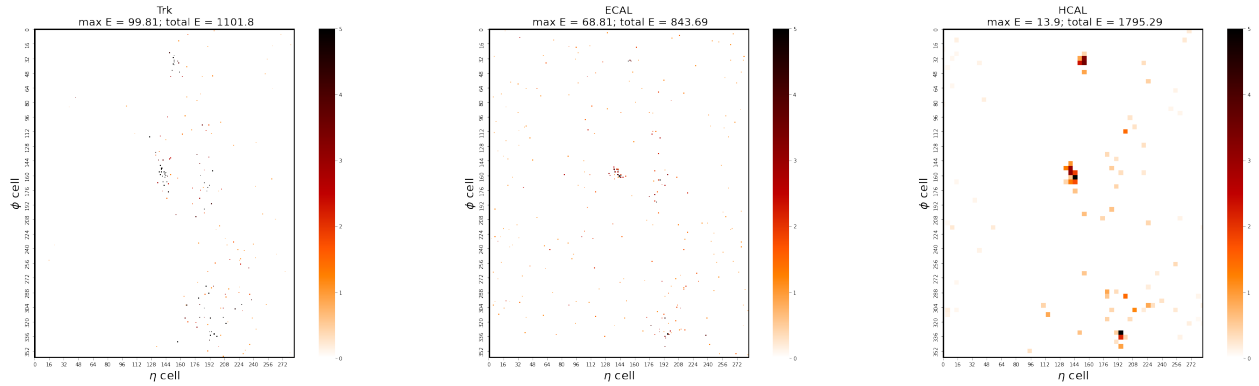


Figure 7: E_T deposits for a SVJ(3.1 TeV) event in the inner tracker (left), ECAL (middle), and HCAL (right).

- The image tokenizer is a two-layer CNN. Each convolutional layer has a 3×3 kernel, ReLU activation [82] and he_normal initialization of weights, which is then followed by overlapping max-pooling (3×3 kernel with stride 2).
- The CCT is made of two transformer blocks [55]. Each block has two heads in the multi-head attention layers, with 128 projection units, layer normalization [83] and a 10% dropout rate. The attention layers are followed by a multi-layer perceptron (MLP) with skip connections. Each MLP has two layers with 128 units, 20%

dropout rate, and GELU [84] activation. The skip connections are regularized by stochastic depth [85] with a 20% drop rate.

The model outputs the logits for our three classes (QCD, SUEPs and SVJs), resulting in about 400k parameters. We trained the CCT for 30 epochs with a batch size of 128 and our image augmentations. The model is optimized by AdamW with our default hyperparameters. Model selection is performed according to the AUROC.

A.4 AE Architecture

Table 9 describes the architecture of the AE model inspired by [8] that we used to compare against our CoDAE models. The AE has 600k parameters, a latent space of size 32, and was trained to minimize the MSE loss on augmented mask images for 50 epochs by the AdamW optimizer.

Encoder	Layer	Filters	Decoder	Layer	Filters
$72 \times 58 \times 1$	conv2d	10	32	dense	100
$72 \times 58 \times 10$	avg_pool	-	100	dense	400
$36 \times 29 \times 10$	conv2d	5	400	reshape	-
$36 \times 29 \times 5$	conv2d	5	$20 \times 20 \times 1$	conv_t	5
$36 \times 29 \times 5$	avg_pool	-	$40 \times 40 \times 5$	conv2d	5
$18 \times 14 \times 5$	flatten	-	$40 \times 40 \times 5$	conv_t	5
1260	dense	400	$80 \times 80 \times 5$	conv2d	5
400	dense	100	$80 \times 80 \times 5$	crop	-
100	dense	32	$72 \times 58 \times 5$	conv2d	1

Table 9: Encoder and decoder architectures of the AE model, inspired by figure 2 in [8]. In particular: conv2d denotes a convolutional layer with a 3×3 kernel, avg_pool a 2×2 average pooling operation, and conv_t a 3×3 transposed convolution [86]. After each convolutional, dense, and transposed convolutional layer we apply the PReLU [75] activation.

A.5 Complete Anomaly Detection Results

In tables 10 and 11 we report the evaluation results for all the anomaly scores we have defined in section 4.4.

Model	SUEP (GeV)							SVJ (TeV)			
	125	200	300	400	700	1000	mAUC	2.1	3.1	4.1	mAUC
CoDAE (Z_1)	79.17	93.14	98.62	99.71	99.95	99.94	95.09	83.37	88.07	90.49	87.31
Z_2	29.13	10.15	2.01	0.44	0.08	0.08	6.98	20.76	15.97	13.15	16.62
Dice	87.43	96.96	99.5	99.89	99.98	99.98	97.29	85.13	88.8	90.9	88.28
BCE	86.43	96.82	99.5	99.91	99.98	99.98	97.1	85.72	89.94	92.14	89.26
SSE	86.23	96.71	99.48	99.91	99.98	99.98	97.05	85.5	89.67	91.87	89.01
PixelSum	79.96	93.78	98.81	99.75	99.95	99.95	95.37	83.36	88.52	91.09	87.66
SAE (mask)	79.4	93.39	98.73	99.74	99.96	99.95	95.19	83.09	88.48	91.17	87.58
SAE	33.47	29.74	40.89	62.67	95.33	95.45	59.59	35.78	42.95	51.16	43.3
Cat. CoDVAE (Z_1)	77.54	91.5	97.71	99.21	99.42	99.19	94.1	81.36	86.4	88.9	85.55
Z_2	22.78	8.18	1.86	0.48	0.21	0.33	5.64	17.28	12.24	9.71	13.08
KL (reverse)	65.93	79.99	90.61	95.02	97.8	98.07	87.9	76.82	81.32	83.35	80.5
KL (forward)	69.32	83.92	93.18	96.38	98.04	98.18	89.84	79.69	84.08	86.11	83.3
Dice	87.25	96.94	99.51	99.9	99.98	99.98	97.26	84.08	88.29	90.56	87.64
BCE	86.89	96.98	99.5	99.9	99.98	99.98	97.21	85.26	89.76	92.03	89.02
SSE	86.93	97.01	99.51	99.9	99.98	99.98	97.22	85.29	89.78	92.04	89.04
PixelSum	78.12	90.52	96.37	97.98	96.59	93.5	92.18	82.19	87.7	90.39	86.76
SAE	63.3	87.58	98.38	99.77	99.94	99.94	91.49	70.25	76.3	80.75	75.77
AE [8]-like (Dice)	33.01	37.27	40.64	42.54	40.5	36.12	38.35	49.43	39.43	32.23	40.36
BCE	77.9	92.22	98.24	99.61	99.93	99.93	94.64	82.73	87.22	89.44	86.46
SSE	75.34	91.08	98.1	99.6	99.93	99.93	94.0	82.09	86.64	88.89	85.87
PixelSum	83.89	94.6	98.69	99.68	99.95	99.94	96.13	83.26	88.72	91.44	87.81
SAE	77.89	92.22	98.24	99.61	99.93	99.93	94.64	82.73	87.22	89.44	86.46
SAE (mask)	20.6	6.61	1.27	0.26	0.04	0.05	4.81	16.91	11.52	8.83	12.42
Dirichlet VAE [21] (Z_1)	52.88	53.13	52.74	51.84	49.84	49.13	51.59	45.53	44.77	44.7	45.0
Z_2	51.93	54.99	59.58	63.17	71.16	74.51	62.55	63.52	67.37	69.26	66.72
Z_3	51.65	50.9	49.72	48.95	47.13	46.57	49.15	46.64	46.08	45.33	46.02

Table 10: Complete anomaly detection results on test-set. AUROC metric, higher is better.

Model	SUEP (GeV)							SVJ (TeV)			
	125	200	300	400	700	1000	mFPR	2.1	3.1	4.1	mFPR
CoDAE (Z_1)	11.95	2.535	0.228	0.022	0.001	0.001	2.46	4.541	1.988	1.144	2.56
Z_2	69.96	91.71	99.05	99.89	99.99	99.99	93.43	82.63	89.32	92.8	88.25
Dice	5.837	0.764	0.063	0.003	~ 0	~ 0	1.11	2.999	1.429	0.854	1.76
BCE	7.292	1.108	0.078	0.004	~ 0	~ 0	1.41	3.047	1.214	0.636	1.63
SSE	7.471	1.164	0.09	0.006	~ 0	~ 0	1.46	3.158	1.278	0.688	1.71
PixelSum	10.16	1.944	0.142	0.009	~ 0	~ 0	2.04	4.197	1.625	0.776	2.2
SAE (mask)	10.53	2.088	0.146	0.009	~ 0	~ 0	2.13	4.354	1.579	0.696	2.21
SAE	67.45	76.24	54.68	0.594	~ 0	~ 0	33.16	62.97	50.67	31.55	48.4
Cat. CoDVAE (Z_1)	12.91	3.329	0.575	0.219	0.227	0.341	2.93	5.9	2.866	1.85	3.54
Z_2	76.85	93.59	99.27	99.87	99.89	99.77	94.87	86.57	92.91	95.39	91.62
KL (reverse)	21.76	9.606	3.019	1.218	0.182	0.098	5.98	9.696	6.602	5.542	7.28
KL (forward)	19.08	7.498	2.635	1.452	0.739	0.677	5.35	7.425	4.913	4.085	5.47
Dice	5.252	0.603	0.034	0.004	~ 0	~ 0	0.98	3.463	1.502	0.81	1.92
BCE	6.655	0.954	0.072	0.007	~ 0	~ 0	1.28	3.073	1.177	0.59	1.61
SSE	6.652	0.944	0.071	0.007	~ 0	~ 0	1.28	3.065	1.176	0.588	1.61
PixelSum	12.01	3.851	1.147	0.765	1.688	3.189	3.77	5.528	2.456	1.451	3.15
SAE	13.5	1.063	0.048	0.003	~ 0	~ 0	2.44	6.006	1.872	0.76	2.88
AE [8]-like (Dice)	63.79	57.04	52.05	49.48	52.99	59.42	55.8	41.47	56.06	66.91	54.82
BCE	11.99	2.551	0.213	0.024	~ 0	~ 0	2.46	4.61	2.085	1.228	2.64
SSE	13.48	2.86	0.229	0.014	~ 0	~ 0	2.76	5.012	2.277	1.288	2.86
PixelSum	8.22	1.904	0.211	0.035	~ 0	~ 0	1.73	4.346	1.74	0.863	2.32
SAE (mask)	80.06	95.39	99.58	99.96	100.0	100.0	95.83	87.33	93.98	96.6	92.63
SAE	11.99	2.551	0.213	0.024	~ 0	~ 0	2.46	4.613	2.085	1.23	2.64
Dirichlet VAE [21] (Z_1)	25.49	21.03	15.29	13.72	11.2	11.12	16.31	44.39	44.72	44.9	44.67
Z_2	26.06	17.38	10.15	6.66	2.572	1.42	10.71	21.42	14.89	10.92	15.74
Z_3	28.31	24.23	19.91	17.12	14.87	14.23	19.78	41.6	42.3	43.12	42.34

Table 11: Complete anomaly detection results on test-set. FPR40 metric, lower is better.